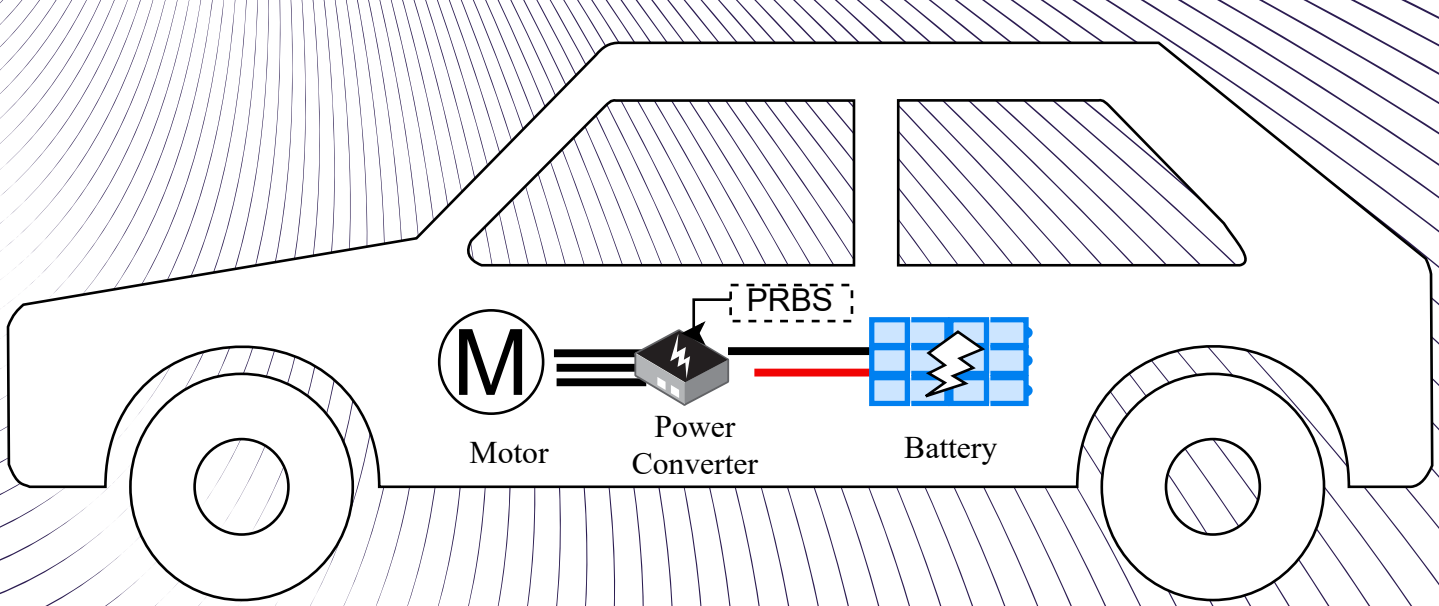

Online Battery Impedance Spectroscopy Using Pseudo-Random Binary Sequence

Anton Hviid Olsen, Bhupal Khatiwada, Lierni Altuna Aristizabal

PED3-940

Power Electronics and Drives, 3rd Semester

AALBORG UNIVERSITY
STUDENT REPORT

Third Semester Power Electronics and Drives
Pontoppidanstræde 111
9220 Aalborg Øst

Title:

Online Battery Impedance Spectroscopy Using Pseudo-Random Binary Sequence

Theme:

Project in Advanced Energy Systems

Project period:

September-December 2025

Project group:

PED3-940

Participants:

Anton Hviid Olsen
Bhupal Khatiwada
Lierni Altuna Aristizabal

Supervisor:

Erik Schaltz

Pages: 56
Due date: 19/12/2025

Abstract:

Nowadays, electric vehicles (EVs) are becoming increasingly widespread. Consequently, there is a growing desire to obtain a better understand of their batteries both with respect to degradation and remaining capacity. Therefore, the aim of this project is to obtain the Nyquist plot of a battery while it is running a Permanent Magnet Synchronous Machine (PMSM) using an inverter. It is investigated whether a Pseudo-Random Binary Sequence (PRBS) could be a possible solution for this, since it produces a broad span of frequencies with the same magnitude, similar to Electrochemical Impedance Spectroscopy (EIS), without having to implement any costly hardware. For this purpose, a model containing a battery, inverter and PMSM with Field Oriented Control (FOC) is constructed, where the PRBS is applied in the d-current reference for minimal impact on the speed. In simulation environment, it was concluded that implementing PRBS is possible, however the method is sensitive to disturbances. Experimental validation was performed, using both 4-bit and 11-bit PRBS, where the method was approved. PRBS was applied to the motor under both stationary and operating conditions, resulting in a similar accuracy in Nyquist plot for operating case despite of the influence of the q-current. Additionally, only part of the Nyquist plot was obtained, due to the inherent nature of the PRBS frequency content. Nevertheless, it was concluded that PRBS can be used for the purpose of obtaining the Nyquist plot of a battery, although with limitations.

Preface

The following project has been completed by 3rd-semester power electronic and drives Engineering students, under the supervision of Erik Schaltz. The authors would like to extend their gratitude to Erik Schaltz for the help and guidance throughout this project.

In this project, tables, equations and figures are used. These are referenced throughout the project. Tables and figures are enumerated and are referenced using their respective number, equations are also enumerated but are referred to as (number) with parenthesis. Literary sources are enumerated and referred to in the form [number]. The number corresponds to a number in the bibliography, where the entire list of sources is compiled. The sources appear in the order that they are used.

If a source citation appears before a period, the source pertains to the preceding sentence. However, the source pertains to the entire paragraph if the citation is placed after a period.

Software used in the project:

- MATLAB
- MATLAB Simulink
- MATLAB Simulink Speedgoat blockset
- Overleaf LaTeX
- Draw.io

Anton Hviid Olsen
ahol21@student.aau.dk

Bhupal Khatiwada
bkhati24@student.aau.dk

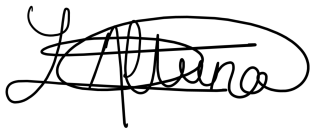

Lierni Altuna Aristizabal
laltun24@student.aau.dk

Aalborg University, 19 December 2025

Nomenclature

Symbols

Symbol	Definition	Unit
C_1	Charge Transfer Capacitance of Battery	[F]
C_2	Diffusion Capacitance of Battery	[F]
f_0	Fundamental Frequency for FFT	[Hz]
G_{CL}	Closed Loop Transfer Function	[−]
G_{OL}	Open Loop Transfer Function	[−]
$G_{pd}(s)$	Plant Equation for d Current	[A/V]
$G_{pq}(s)$	Plant Equation for q Current	[A/V]
I	Current	[A]
I_m	Magnitude of Current	[A]
i_a	Phase a Current	[A]
i_b	Phase b Current	[A]
i_c	Phase C Current	[A]
i_d^*	d axis Reference Current	[A]
i_q^*	q axis Reference Current	[A]
J	Inertia of the Motor	$[\mathrm{kg} \cdot \mathrm{m}^2]$
L_d	Inductance in d axis	[H]
L_q	Inductance in q axis	[H]
N	Total Length of Sequence	[−]
n	Motor Speed	[rpm]
n^*	Motor Speed Reference	[rpm]
n_p	Number of Pole Pairs of a Motor	[−]
P_{in}	Input Power	[W]
P_{out}	Output Power	[W]
P_{total}	Total Power	[W]
R	Resistance	[Ω]
R_0	Ohmic Resistance of a Battery	[Ω]
R_1	Charge Transfer Resistance of a Battery	[Ω]
R_m	Stator Phase Resistance	[Ω]
R_n	N_{th} Resistance Component on a Battery	[Ω]
T_e	Electrical Torque	[Nm]

Continuation of Table

Symbol	Definition	Unit
T_m	Mechanical Torque	[Nm]
T_{period}	Total Time for one Period	[−]
V	Voltage of a Battery	[V]
V_m	Magnitude of Voltage	[V]
$V_n(t)$	Voltage across PMSM in Time Domain	[V]
V_{oc}	Open Circuit Voltage	[V]
V_T	Terminal Voltage	[V]
v^*_{abc}	Reference Voltage in *abc* Frame	[V]
$v_{bat}(t_i)$	Voltage of Battery at Interruption Time t_i	[V]
v_d	Voltage in d-axis	[V]
v^*_d	d-axis Reference Voltage	[V]
v_q	Voltage in q-axis	[V]
v^*_q	q-axis Reference Voltage	[V]
Z_{img}	Imaginary Impedance	[Ω]
Z_{real}	Real Impedance	[Ω]
Z_{tot}	Total Impedance	[Ω]
Z_W	Warburg Impedance	[Ω]
Δt_s	Sampling Time	[s]
ΔV_0	Voltage increment	[V]
δ	Damping Ratio	[−]
λ_n	Stator Flux Linkage	[Wb]
λ_d	Flux Linkage in d-axis	[Wb]
λ_q	Flux Linkage in q-axis	[Wb]
λ_{mpm}	Permanent Magnet Flux Linkage	[Wb]
ω	Angular Speed	[rad/s]
ω^*	Angular Speed Reference	[rad/s]
ω_B	Bandwidth	[Hz]
ω_r, el	Electrical Speed	$\frac{rad}{s}$
θ_i	Current Phase Angle	[°]
θ_v	Voltage Phase Angle	[°]
τ	Time Constant	[s]

End of Table

Acronyms

Acronym	Definition
AAU	Aalborg University
abc	abc Reference Frame
AC	Alternating Current
BMS	Battery Management System
DC	Direct Current
DIBS	Discrete Interval Binary Sequence
EIS	Electro-chemical Impedance Spectroscopy
EMF	Electromotive Force
EMI	Electromagnetic Interference
EU	European Union
EV	Electric Vehicle
FFT	Fast Fourier Transform
FOC	Field Oriented Control
GHG	Green House Gas
I-f	Current Frequency
IRBS	Inverse Repeat Binary Sequence
Li-ion	Lithium Ion
LiFePo4	Lithium - Iron - Phosphate
MLBS	Maximum Length Pseudo Random Binary Sequence
PI	Proportional Integral
PMSM	Permanent Magnet Synchronous Machine
PRBS	Pseudo-Random Binary Sequence
PWM	Pulse Width Modulation
RC	Resistance Capacitance
SoC	State of Charge
SoH	State of Health
SPWM	Sinusoidal Pulse Width Modulation
SRF	Synchronous Reference Frame
V-f	Voltage Frequency
VSC	Voltage Source Converter
XOR	Exclusive OR gate

Contents

1. Introduction

To mitigate the effects of climate change, governments are establishing laws to reduce Greenhouse Gas (GHG) emissions and promote sustainability [1]. In this context, Electric Vehicles (EV) are emerging as a key solution to create more sustainable means of transportation, as transport accounts for 25% of total GHG emissions in the EU and is the main cause of air pollution in urban environments [1]. Therefore, many projects have been carried out to improve their performance and replace combustion engines.

One field of research in EV projects is the battery, as it is one of the main components of the vehicle. Of all battery types, lithium-ion (Li-ion) batteries have become popular in electric vehicles due to their high energy density, long lifetime, and high efficiency. These batteries are most often equipped with a Battery Management System (BMS) that ensures safe operation and monitors temperature, voltage, and current of the battery. Using this data, it is possible to estimate the state of the battery, which includes the State of Charge (SoC) and State of Health (SoH). The SoC is an indication of the available charge in the battery, while the SoH is an indication of the deterioration of the battery.[2]

Therefore, accurate estimations of these parameters are useful for improving battery performance, as they indicate the remaining driving range and lifetime of the battery. However, accurate determination of the SoC and SoH is difficult due to their non-linear dependence on the measured quantities. These non-linearities are a result of the impedance varying with SoH and SoC, which is typically not accounted for by the BMS. [2]

Therefore, it is desired to perform regular measurements of the battery impedance, which the BMS currently does not provide. Since impedance measurements require the battery to be in operation, these measurements should be performed while the EV is operating [3]. This introduces the issue that measurements might cause disturbances in the torque and speed of the motor, which is undesirable. Furthermore, measurements might require additional costly equipment [4]. This is a drawback as it would lead to an increase in the price of an EV.

Based on this, the goal of this project is to perform an online battery impedance measurement without disturbing the performance of the EV and without adding additional costly hardware. As will be seen in the following section, these measurements will be performed using a Pseudo-Random Binary Sequence (PRBS).

2. Problem Analysis

With the overarching problem introduced, this chapter will investigate battery modelling, the current methods of battery parameter determination, and present the components in an EV which must be considered.

2.1 Conventional Methods of Electric Battery Modelling

Conventionally, battery modelling can be categorised into three types: the ideal model, the static model and the dynamic model, as can be seen from Figure 2.1.

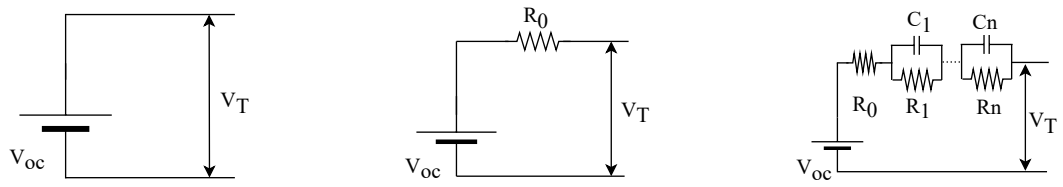

(a) (b) (c)

Figure 2.1: Different electrical representations of a battery: (a) ideal model, (b) static model, and (c) dynamic model. [5, 6]

In the ideal model of Figure 2.1a, only a constant voltage source V_{oc} is considered, so the terminal voltage equals the open-circuit voltage regardless of load, temperature, or SoC [6]. On the other hand, the static model in Figure 2.1b adds internal resistance R_0, which represents the heat loss of the battery [6]. However, these two models represent only the static behaviour of the battery, which cannot accurately represent the real behaviour of the battery.

The dynamic model includes, in addition to R_0 and V_{oc}, several RC branches, as shown in Figure 2.1c. These serve to represent the dynamic behaviour of the battery with respect to transient periods. The resistance and capacitance of these branches are in parallel and the number of branches varies, depending on the accuracy of the model.[7]

The parameter estimation methods are based on the dynamic model, as it provides a more realistic representation of a real battery. Their aim is to obtain the internal impedance of the battery and consequently to determine other parameters of the battery such as the SoC and the SoH. More details on battery modelling can be seen in 4.1.

2.2 Conventional Methods of Parameter Determination of Batteries

This section will present the two most prevalent conventional methods for determining impedance parameters of batteries. These methods include Current interrupting method and Electro-chemical Impedance Spectroscopy (EIS). [3]

2.2.1 Current Interrupting Method

A method of determining the parameters of a battery is the current interrupting method. This method will be explained considering one RC branch for simplification, but it can be used to estimate any RC branches. In Figure 2.2, the voltage response is used to determine the battery parameters when a current step is applied.

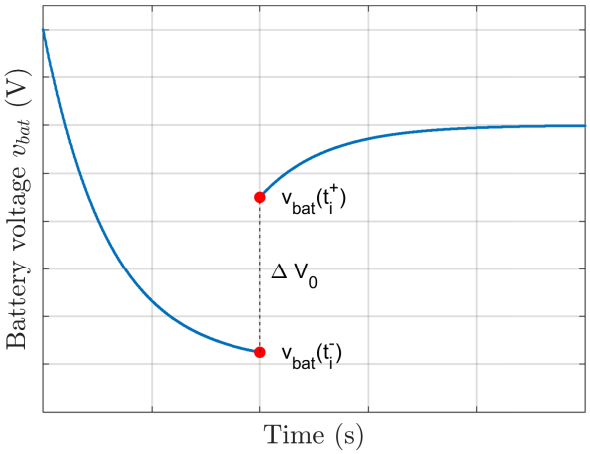

Figure 2.2: General behaviour of the battery under current interrupting method [3].

Firstly, a constant current is discharging the battery for a period, after which it is immediately stopped. It can be seen from Figure 2.2, during the discharge period, the battery voltage gradually decreases. When the discharge period ends, the voltage increases instantaneously by a value denoted as ΔV_0, which can be described as in Equation (2.1). [3]

$$\Delta V_0 = |v_{bat}(t_i^+) - v_{bat}(t_i^-)| \tag{2.1}$$

Where t_i^- and t_i^+ are the instances just prior to and just after t_i, respectively. After the initial voltage increase, the voltage continues to rise, although at a much slower pace, which is caused by the internal capacitances of the battery. The internal resistance can be calculated from ΔV_0 and the current as shown in Equation (2.2). [3]

$$R_0 = \frac{|\Delta V_0|}{|I_{cs}|} \tag{2.2}$$

After the initial current step, the transient voltage response is analysed to determine the parameters of the RC branches. Their values are derived from the exponential behaviour of the voltage and the corresponding time constant τ. By fitting the measured

curve, the expression for the first RC branch is then obtained as: [3]

$$\begin{aligned} R_1 &= \frac{v_1}{I_{cs}(1 - e^{\frac{-\Delta t_{cs}}{\tau}})} \\ C_1 &= \frac{\tau}{R_1} \end{aligned} \tag{2.3}$$

This method requires additional equipment and will disturb operation if done online, since the current is stopped instantaneously, and is therefore unsuitable for the goals of this project.

2.2.2 Electro-chemical Impedance Spectroscopy

In Electro-chemical Impedance Spectroscopy, the impedances of a battery is found using the relation between voltage (V), current (I) and impedance (Z) as seen in Equation (2.4).

$$Z = \frac{I}{V} = \frac{I_m \angle \theta_i}{V_m \angle \theta_v} = R + jX \tag{2.4}$$

Where θ_v and θ_i are the phase angles for voltage and current, respectively, while I_m and V_m are the magnitudes of the current and voltage, and R and X represent resistance and reactance respectively. In fact, this method relies on injecting sinusoidal currents at different frequencies, and by measuring the output voltage and using Equation (2.4), the impedance of the battery can be determined. [3]

If a frequency sweep is conducted for this, which means that measurements are taken at different frequencies at logarithmic intervals, a Nyquist plot can be constructed that shows the resistance on the X-axis and the reactance on the Y-axis, as illustrated in Figure 2.3.

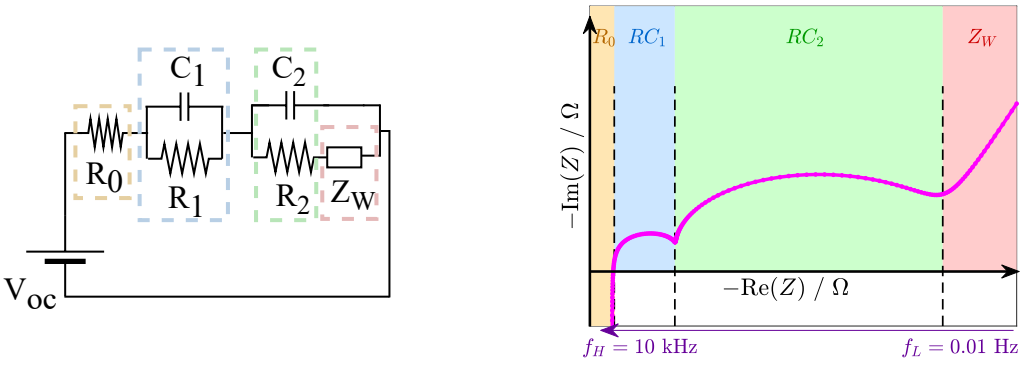

(a) (b)

Figure 2.3: (a) Dynamic electrical model of a battery and its respective (b) Nyquist plot [8].

The plot of Figure 2.3b will vary depending on the State of Charge (SoC) and the State of Health (SoH). Therefore, to achieve accurate data for the battery, this will have to be done regularly to account for deterioration. However, this requires charging and discharging the battery in a certain manner, using expensive equipment and a considerable amount of time, which will not be suitable while driving an EV as it will affect the behaviour. [3]

2.3 PRBS Method

The pseudo-random binary sequence (PRBS) is a broadband injection technique containing different frequencies, which is generated by a binary signal. In linear system identification, binary signals are generally preferred because they provide the strongest possible excitation without exceeding the maximum allowed signal levels in the time domain. Moreover, unlike sinusoidal signals, they offer the practical advantage of being easily generated by low-cost hardware capable of producing only a limited number of output levels. This type of hardware can also be used in real-time applications, allowing online measurement of battery impedance. For these reasons, this project will implement a PRBS-based method to determine the battery impedance. [9, 10]

The PRBS signal is used as the current reference to charge or discharge the battery, after which the DC voltage and current of the battery are measured. By applying the Fast Fourier Transform (FFT) to these measurements, the frequency response of the battery is obtained. Using the FFT of both signals, a Nyquist plot can be generated, which should be identical to the Nyquist plot produced using the EIS method, shown in Figure 2.3b. [9]

2.3.1 Different types of PRBS

There are different types of PRBS method [10]:

- Maximum-length pseudo-random binary sequence (MLBS)
- Inverse-repeat binary sequence (IRBS)
- Discrete-interval binary sequence (DIBS)
- Orthogonal binary sequences

The Maximum-length pseudo-random binary sequence (MLBS) is among the most widely used PRBS signals. It is periodic and controllable, making it a versatile method for many practical applications in system parametrisation. Therefore, this project will focus on this type of binary sequence. To avoid confusion, the term PRBS will represent MLBS throughout the project. Further explanations regarding this method is presented in Chapter 4. [9, 10]

2.3.2 Current PRBS Application Methods into Battery Systems

Currently, the PRBS method has been implemented in batteries in different ways [11]:

- Switching-resistor method: In this method, a switch and a resistor connected in series are placed in parallel with the battery. The two-level PRBS signal, corresponding to the ON and OFF states in this method, is applied directly to the switch. Assuming that the resistor has a sufficiently high value, the small perturbed signal is sent directly to the battery.
- Linear-transformer method: In this method, a linear transformer is inserted between the battery and the load. The PRBS perturbation is injected through the

AC nominal voltage of the transformer, which subsequently induces a current. This induced current excites the battery impedance, which can then be measured and characterised.

- Current-load method: In this method, the battery is connected to a load, which can be a power drive system together with a power electronic converter. The current excited by the PRBS is applied online through the load, which generates an excitation waveform with the specified amplitude and frequency into the battery.

Since this project focuses on EV applications, where a motor and an inverter are present, the PRBS perturbation will be injected through motor control. Therefore, the current-load method will be used due to its simplicity and suitability for this project.

2.4 The Drive System

As mentioned above, to drive an EV, it is essential to have a motor connected to the battery using an inverter as shown in Figure 2.4. The motor is a PMSM motor since it allows efficient torque and speed control when powered through the inverter. Through the inverter, the PRBS signal is injected into the motor, which influences the battery.

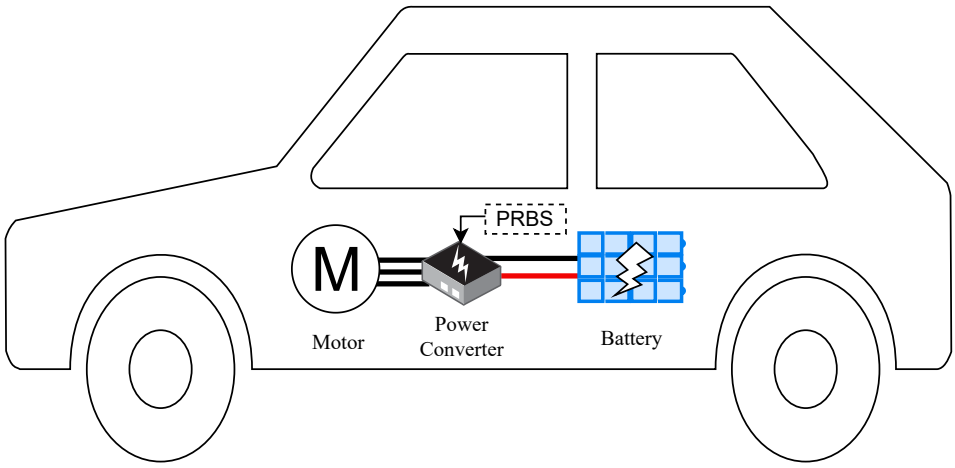

Figure 2.4: Powertrain of an EV with PRBS injected.

However, adding the PRBS could be problematic since it introduces additional frequencies in the system. Therefore, the challenge of this project is to add the PRBS signal in the current reference of the motor without perturbing the operation of the motor but still be capable of exciting the battery enough to obtain its Nyquist plot.

3. Problem Statement

In the previous chapter, it has been explained that PRBS may have benefits in determining the Nyquist plot of a battery while running the motor in EVs. This will improve the understanding of each battery, leading to a better use of the resources. Therefore, this project aims to answer the following problem statement:

Can the PRBS online method for obtaining the Nyquist plot of a battery be implemented in a drive system while disturbing the PMSM operation minimally?

Based on the problem statement, the project will be divided into the following topics:

- How is PRBS generated and how can it be used to obtain the Nyquist plot of a battery?
- How can a model be constructed in Simulink to simulate a drive system utilising the PRBS method as an onboard battery parameter determination system?
- How can a physical setup be constructed to validate the findings of the system model and obtain the Nyquist plot of a battery?

3.1 Scope of the Project

In this project, the focus is on obtaining Nyquist plots. Further analysis will not be conducted, such as estimation of SoC and SoH from the Nyquist plot, but could be relevant for a future project.

3.2 Assumptions

- In this project, due to time constraints and to increase simplicity, the PMSM is considered to be non-salient, although this might not be the case.
- The inertia value of the PMSM used in this project for the simulation is assumed to be $4.58 \cdot 10^{-3}\text{kgm}^2$.

4. Modelling

In this chapter, the modelling performed and the control implemented will be presented. The modelling consists of a battery model, a PMSM model and a model of PRBS generation. These models are constructed to develop the control and parametrisation technique, and to provide a realistic system behaviour from which to draw conclusions. Field Oriented Control (FOC) is implemented on the PMSM to accurately regulate current and speed of the motor. Finally, a complete model will be developed such that simulations can be conducted before laboratory validation is performed in the subsequent chapters.

4.1 Battery Modelling

When applying PRBS in EV applications, the aim is to obtain the frequency-dependent impedance of the battery. In this project, two RC branches are considered, as illustrated in Figure 4.1.

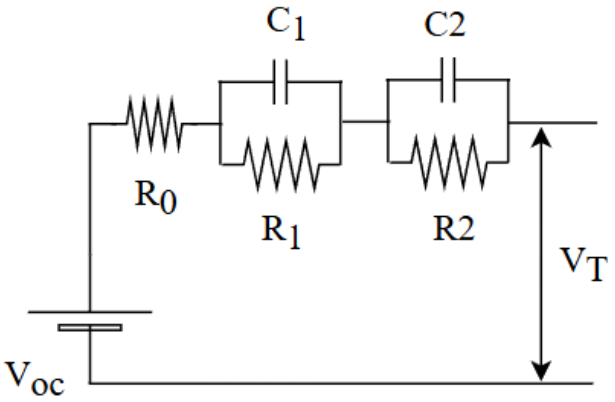

Figure 4.1: Dynamic model of a battery with two RC branch.

Where, C_1 is the charge transfer capacitance which determines the high frequency behaviour, while C_2 is the diffusion capacitance which determines the low frequency behaviour. Likewise, R_1 is the charge transfer resistance, which is most dominant at high frequencies, while the diffusion resistance, R_2, is most prevalent at low frequencies. R_0 is the minimal resistance of the battery [12]. The influence of each component in the Nyquist plot is shown in Figure 2.3.

Consequently, the equivalent impedance of the battery can be expressed as shown in Equation (4.1) [13].

$$Z_{tot} = R_0 + \left(\frac{1}{R_1} + j\omega C_1\right)^{-1} + \left(\frac{1}{R_2} + j\omega C_2\right)^{-1} \tag{4.1}$$

Where Z_{tot} is total equivalent impedance and ω is the angular frequency. This expression can be simplified to become an Equation (4.2).

$$Z_{tot} = R_0 + \frac{R_1(1 - j\omega R_1 C_1)}{1 + \omega^2 R_1^2 C_1^2} + \frac{R_2(1 - j\omega R_2 C_2)}{1 + \omega^2 R_2^2 C_2^2} \tag{4.2}$$

Equation (4.2) consists of a real and an imaginary part, which are separated and shown in Equation (4.3).

$$\begin{aligned} Z_{real} &= R_0 + \frac{R_1}{1 + \omega^2 R_1^2 C_1^2} + \frac{R_2}{1 + \omega^2 R_2^2 C_2^2} \\ Z_{img} &= -\frac{\omega R_1^2 C_1}{1 + \omega^2 R_1^2 C_1^2} - \frac{\omega R_2^2 C_2}{1 + \omega^2 R_2^2 C_2^2} \end{aligned} \tag{4.3}$$

From Equation (4.3) it is evident that both the resistive and reactive parts are frequency dependent. If a frequency sweep is performed for this equivalent impedance, a Nyquist plot can be obtained, where the resistive part is on the X-axis and the reactive part is on the Y-axis, as mentioned in Section 2.2.2.

4.1.1 Selection of Impedance Parameters and Nyquist Plot

To obtain a set of realistic impedance parameters to use in the model, experimental EIS data from AAU energy is used [14]. The aim is to insert these values into the model and using the PRBS method, the same values should be extracted. This will validate the method for the battery parametrisation in simulation environment. A conclusive validation can then be done in a laboratory environment.

Firstly, the EIS data from AAU is plotted, as shown in Figure 4.2.

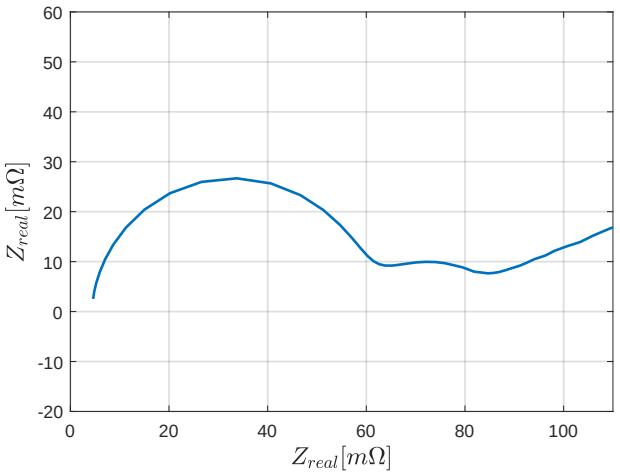

Figure 4.2: Nyquist plot based on EIS data from AS1868117 at 5°C and an SoC of 90%.

From this Figure 4.2, R_0 can be extracted directly, as it is the value where the first semicircle crosses the real axis. For the calculation of the resistance and capacitance,

a few additional steps are required.

Firstly, the leftmost semicircle of the Nyquist plot is considered. Two adjacent points on the surface of this semicircle are selected, which lie nearly at the top of the semicircle to determine the corresponding resistance and capacitance values. These points are chosen because the first RC branch is dominant at its corresponding peak. For this reason, the second RC branch can be neglected, and therefore the impedance at the point can be calculated as seen in Equation (4.4). [15]

$$|Z| = \sqrt{Z_{real}^2 + Z_{img}^2} = \frac{1}{\sqrt{\frac{1}{R^2} + (\omega \cdot C)^2}} \tag{4.4}$$

If the two chosen points are then subtracted from each other, as shown in Equation (4.5a), it is possible to isolate for the capacitance, as can be seen in Equation (4.5b).

$$|Z_1| - |Z_2| = \frac{1}{\sqrt{\frac{1}{R_1^2} + (\omega_1 C_1)^2}} - \frac{1}{\sqrt{\frac{1}{R_1^2} + (\omega_2 C_1)^2}}, \tag{4.5a}$$

$$C_1 = \sqrt{\frac{\frac{1}{|Z_2^2|} - \frac{1}{|Z_1^2|}}{\omega_2^2 - \omega_1^2}}. \tag{4.5b}$$

Where Z_2 and Z_1 are the impedances of the two points, and ω_2 and ω_1 are their corresponding angular frequencies, all of which are known from the data. Knowing the capacitance value in the leftmost semicircle, its resistance value can be calculated using Equation 4.4 [15].

For the second semicircle, this method cannot be replicated, as the second RC branch cannot be assumed to be dominant due to the high influence of the first RC branch. Therefore, the values were determined iteratively.

Using this procedure yields the impedance parameter values shown in Table 4.1.

Table 4.1: Estimated impedance parameters of AS1868117 at 5°C and an SoC of 90%.

Resistors (Ω)			**Capacitors (F)**	
R_0	R_1	R_2	C_1	C_2
0.004613	0.0566	0.0214	0.0067	0.7826

Using the impedance parameters obtained as shown in Table 4.1, the Nyquist plot is made using Equation 4.3 which is shown in Figure 4.3.

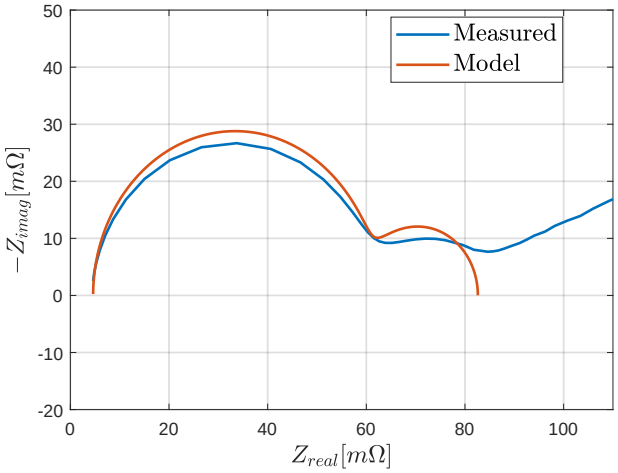

Figure 4.3: Measured and estimated Nyquist plot of AS1868117.

In Figure 4.3, it can be seen that the first semicircles are nearly identical, indicating that the theoretical and experimental impedance values correspond well in the high-frequency range. However, in the second RC branch, the estimated and measured impedance values do not align as closely in the low-frequency region. This difference may arise from the exclusion of the third region, due to the assumption of two RC branches per cell. Nevertheless, this inaccurate fit does not influence the project, since the goal is to investigate the feasibility of the PRBS method; as such, it should work for any battery parameters.

4.2 Modelling of the PMSM

The relationship between voltage and current for a PMSM is obtained from the general voltage equation of an electrical machine, shown in Equation (4.6). Hence, the impedance of a PMSM consists both of a magnetic part and a resistive part. [16]

$$V_n(t) = R_m i_n(t) + \frac{d\lambda_n(t)}{dt} \tag{4.6}$$

Where R_m is the stator phase resistance, λ_n is the phase stator flux linkages and the subscript n denotes either phase a, b or c. In this equation, the components are sinusoidal, which makes them challenging to control with PI controllers. Therefore, the equation is transformed into the synchronous reference frame (SRF), where the sinusoidal components become DC terms that rotate at an electrical angular velocity of $\omega_{r,el}$. The transformations consist of the Clarke and Park transformations, which are combined in the transformation matrix denoted as K_{abc2dq}, shown below: [16]

$$K_{abc2dq} = \begin{bmatrix} \cos(\theta) & \cos\left(\theta - \frac{2}{3}\pi\right) & \cos\left(\theta + \frac{2}{3}\pi\right) \\ \sin(\theta) & \sin\left(\theta - \frac{2}{3}\pi\right) & \sin\left(\theta + \frac{2}{3}\pi\right) \\ \frac{1}{2} & \frac{1}{2} & \frac{1}{2} \end{bmatrix} \tag{4.7}$$

Using this matrix, Equation (4.6) becomes:

$$\begin{bmatrix} v_d \\ v_q \\ v_0 \end{bmatrix} = K_{abc2dq} R_m \begin{bmatrix} i_a \\ i_b \\ i_c \end{bmatrix} + K_{abc2dq} \frac{d}{dt} \begin{bmatrix} \lambda_a \\ \lambda_b \\ \lambda_c \end{bmatrix} \tag{4.8}$$

Then, by multiplying by $K_{abc2dq} K_{abc2dq}^{-1}$ on the rightmost term and simplifying, the expression becomes:

$$\begin{bmatrix} v_d \\ v_q \\ v_0 \end{bmatrix} = R_m \begin{bmatrix} i_d \\ i_q \\ i_0 \end{bmatrix} + \frac{d}{dt} \begin{bmatrix} \lambda_d \\ \lambda_q \\ \lambda_0 \end{bmatrix} + \begin{bmatrix} 0 & \omega_{r,el} & 0 \\ -\omega_{r,el} & 0 & 0 \\ 0 & 0 & 0 \end{bmatrix} \begin{bmatrix} \lambda_d \\ \lambda_q \\ \lambda_0 \end{bmatrix} \tag{4.9}$$

Hence, from Equation (4.9), the dq voltage equations for a PMSM can be obtained as shown below:

$$\begin{aligned} v_d &= R_m i_d + \frac{d\lambda_d}{dt} + \omega_{r,el} \lambda_q \\ v_q &= R_m i_q + \frac{d\lambda_q}{dt} - \omega_{r,el} \lambda_d \end{aligned} \tag{4.10}$$

Where v_q and v_d are the q- and d-axis stator voltages, i_q and i_d are the stator currents in the dq frame, and λ_d and λ_q are the d- and q-axis flux linkages. The stator flux linkage terms are given as shown below: [16]

$$\begin{aligned} \lambda_q &= L_q i_q \\ \lambda_d &= L_d i_d + \lambda_{mpm} \end{aligned} \tag{4.11}$$

Where L_d and L_q are the d- and q-axis inductances and λ_{mpm} is the permanent magnet flux linkage. [16]

The power generated by a PMSM is expressed as:

$$P_{mec} = \frac{3}{2} \omega_{r,el} (\lambda_d i_q - \lambda_q i_d) \tag{4.12}$$

Since the power is related to the electromagnetic torque by

$$P_{mec} = T_e \omega_{r,mec} \tag{4.13}$$

The electromagnetic torque of the PMSM can be expressed as:

$$T_e = \frac{3}{2} n_p (\lambda_{mpm} i_q + (L_d - L_q) i_d i_q) \tag{4.14}$$

Where, n_p is the number of pole pairs in the motor and T_e is the electrical torque. As can be seen, i_q is dominant compared to i_d, especially when the motor is close to non-salient. The electromagnetic torque in combination with the load torque determines the angular acceleration of the rotor, as expressed by:

$$J \frac{d\omega_m}{dt} = T_e - T_m \tag{4.15}$$

Where ω_m is the speed, J is the inertia of the motor and T_m is the load torque.

4.3 Control Structure of PMSM

Inserting Equations (4.11) into Equations (4.10), and transforming to the Laplace domain, it can be seen that the two equations are coupled through the back-EMF on the rightmost term of each equation. To be able to control the d and q currents independently, the control structure must compensate for these coupling terms by subtracting them, as shown in Equations (4.16).

$$\begin{aligned} v_d &= R_m i_d + sL_d i_d + \omega L_q i_q - \omega L_q i_q \\ v_q &= R_m i_q + sL_q i_q - \omega(L_d i_d + \lambda_{mpm}) + \omega(L_d i_d + \lambda_{mpm}) \end{aligned} \tag{4.16}$$

Therefore, in the control structure, the voltage equations simplify to:

$$\begin{aligned} v_d &= R_m i_d + sL_d i_d \\ v_q &= R_m i_q + sL_q i_q \end{aligned} \tag{4.17}$$

With these SRF voltages equations, the plant transfer functions can be derived as shown below, where $G_{pd}(s)$ and $G_{pq}(s)$ are the plants for the d and q currents respectively.

$$\begin{aligned} G_{pd}(s) &= \frac{i_d}{v_d} = \frac{1}{sL_d + R_m} \\ G_{pq}(s) &= \frac{i_q}{v_q} = \frac{1}{sL_q + R_m} \end{aligned} \tag{4.18}$$

Using these plant functions, a control diagram for the inner current loop can be drawn, as shown in Figure 4.4. Here, the superscript * denotes that the signal is a reference value.

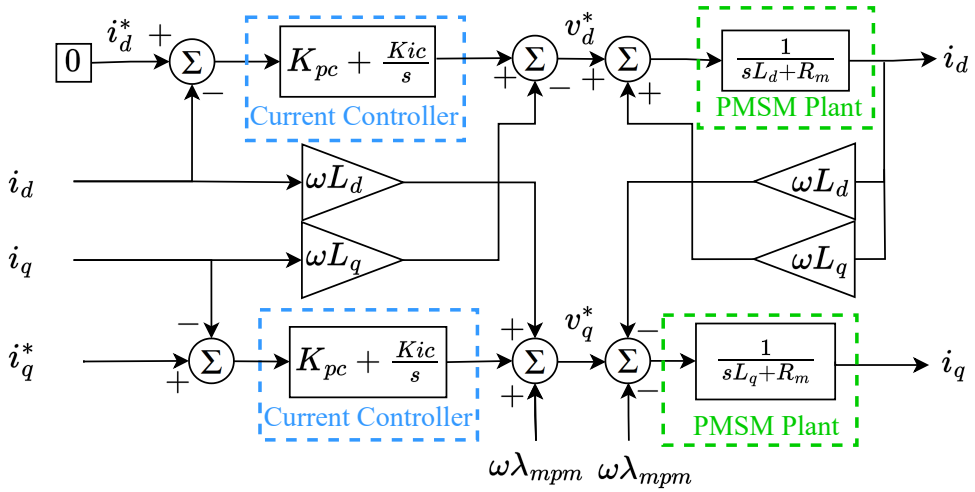

Figure 4.4: Control diagram for the inner current control loop with decoupling terms.

As can be seen in Figure 4.4, both coupling and decoupling terms are included, which means that they cancel each other out.

Once the current loop is defined, the outer speed loop has to be constructed. For this, a few assumptions are made. The first assumption is that the PMSM is non-salient, meaning $L_d = L_q$. Therefore, when considering Equation (4.14), the second term in the parenthesis become zero and the electrical torque can be described as in Equation (4.19).

$$T_e = \frac{2}{3} n_p \lambda_{mpm} i_q \tag{4.19}$$

Consequently, the electrical torque is proportional to the i_q current. Moreover, based on (4.15), the motor speed is directly determined by the electromagnetic torque. Therefore, to regulate the motor speed, it is sufficient to provide the correct i_q reference to the inner current loop. This is achieved using a PI controller in the outer speed loop, as illustrated in Figure 4.5. [16]

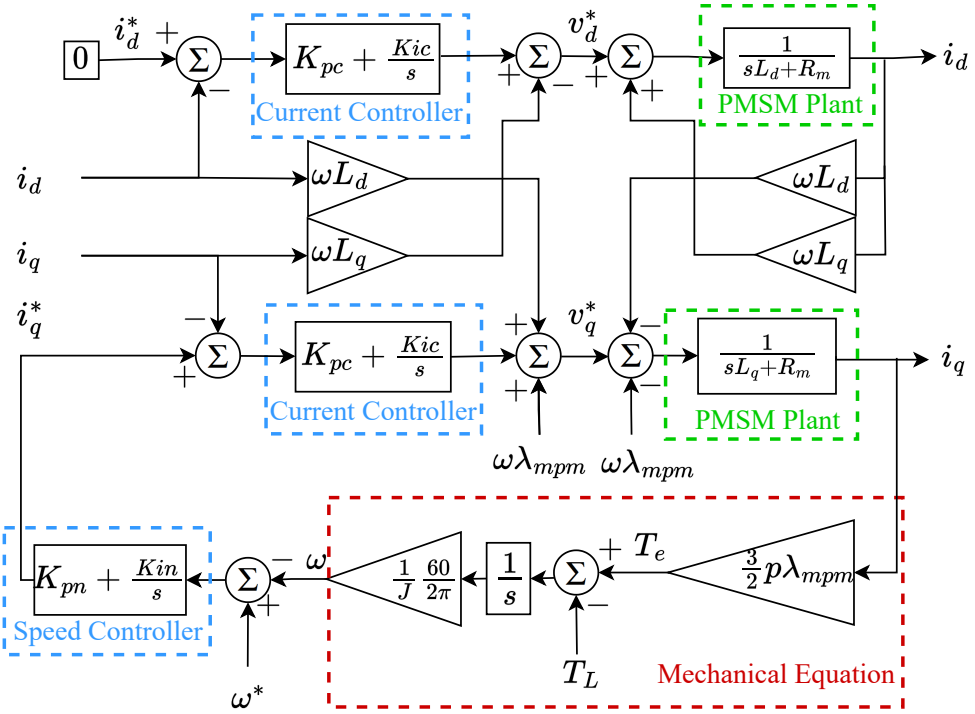

Figure 4.5: Control diagram for the inner current control loop with decoupling terms and the outer speed control loop.

In this setup, the i_d reference would often times be set to zero, as its influence on the speed is small.

4.4 Generation of PRBS

As mentioned previously, this project aims to implement PRBS for battery parametrisation. PRBS has the property that the frequency content has equal magnitude up to a certain level at all multiples of the fundamental frequency, which enables the measurement of the frequency response of the battery. Consequently, the internal impedance can be determined, because the wide range of frequency components produced by the PRBS is equivalent to performing a frequency sweep. [11]

4.4.1 Operation Principle of PRBS

PRBS produces a sequence of ones and zeros, which are seemingly random, but is periodic and predetermined based on the specific configuration. In this section, the basic operation of the PRBS will be explained with a 4-bit shift register shown in Figure 4.6, but the bit number must be selected depending on the application. Therefore, although the basics are explained with 4-bits, the implementation will be with a higher bit number. [17]

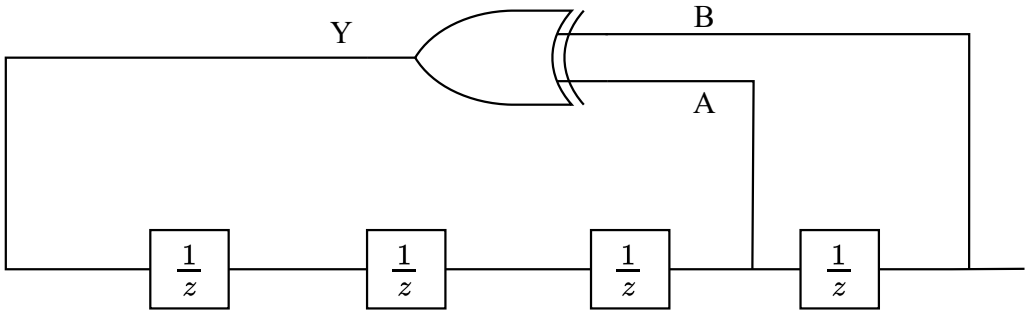

Figure 4.6: PRBS generation using an 4-bit shift register with XOR feedback [10].

Depending on the number of bits, the length of the sequence will be different as defined below:

$$N = 2^n - 1 \tag{4.20}$$

Where n is the number of stages, and N is the length of the sequence [17]. The bit sequence is generated with a shift register using XOR feedback. The XOR feedback takes two bit values and combines them, as illustrated in Figure 4.7. The result is then inserted into the first position of the register, while the remaining values are shifted to the right, forming a new sequence. It should be underlined that the register sequence can be started with any bit combination except all zeros, since this combination will not produce any ones due to the XOR feedback.

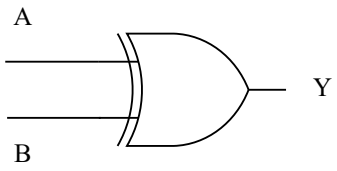

A	B	Y=A'B+AB'
0	0	0
0	1	1
1	0	1
1	1	0

Figure 4.7: XOR logic table.

For example, for the 4-bit structure shown in Figure 4.6 using [0 0 0 1] initial sequence, the register sequence is given in Table 4.2. As seen in Figure 4.6, the fourth stage is connected to the output, so its bit sequence will result in the PRBS output shown in Figure 4.8.

Table 4.2: PRBS sequence for a 4-bit sequence [10].

Shift	Stage 1	Stage 2	Stage 3	Stage 4
1	0	0	0	1
2	1	0	0	0
3	0	1	0	0
4	0	0	1	0
5	1	0	0	1
6	1	1	0	0
7	0	1	1	0
8	1	0	1	1
9	0	1	0	1
10	1	0	1	0
11	1	1	0	1
12	1	1	1	0
13	1	1	1	1
14	0	1	1	1
15	0	0	1	1
16	0	0	0	1

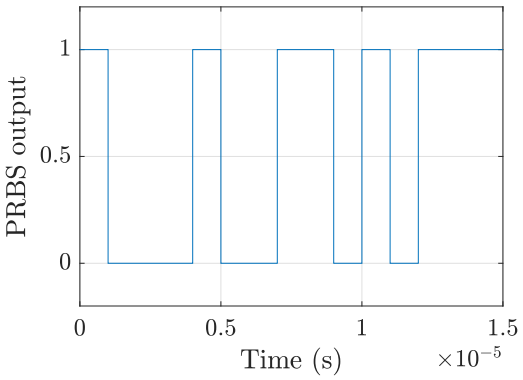

Figure 4.8: PRBS output for a 4-bit sequence.

The sequence created by the XOR repeats periodically based on the PRBS clock and the length of the sequence. In the example illustrated in Figure 4.8, a clock speed 1 MHz and a sequence length of 15 is used. Therefore, the time for each period is as shown below:

$$T_{period} = N \cdot \Delta t_s = 15 \cdot 10^{-6}\text{s} \tag{4.21}$$

Where Δt_s is the sampling time defined by the clock, meaning the time it takes the PRBS to move to another stage in the sequence. Thus, the sequence repeats every 15 μs.

4.4.2 Design of the PRBS Structure

When designing the PRBS generator, it is essential to consider both the number of bits and the positioning of the legs for the XOR feedback. The position of the feedback branches on the XOR needs to follow some criteria, so that a full length sequence is created:

- Branch B at the output: If the feedback loop does not consider the last bit, not all the bits will be inside a loop. Therefore, the sequences will be shorter and end before reaching the full length of N.
- Avoid symmetrical structures with branch A: If the branch A is after the n/2 bit, the distance between branch A and B are equal. This is problematic because it can introduce repetitions in the output sequence. As a result, the sequence is finished before reaching the full length of N, and not all possible sequences are produced.

Therefore, the XOR feedback defines to an extend the frequency of the PRBS, since a short PRBS sequence will result in lower frequency. The bit number also determines the frequencies present when computing the FFT, as it defines the maximum length of the sequence. More generally, the relationship can be the described as:

$$f_0 = \frac{1}{\Delta t_s(2^n - 1)} \tag{4.22}$$

Where f_0 is the fundamental frequency when computing the FFT. It can be calculated using Equation (4.22) because this is the frequency with which the PRBS sequence repeats, meaning it represents the slowest frequency present.

If f_0 is applied to the FFT of the PRBS, it has the characteristic that all multiples of f_0 have almost the same magnitude as the previous one. For this reason, the resolution of the FFT when determining the battery Nyquist plot will depend on f_0. Therefore, f_0 is desired to be as low as possible. Figure 4.9 shows a 11-bit PRBS with a sampling time of 10^{-3} s and its corresponding FFT plot, using $f_0 = \frac{1}{10^{-3}(2^1-1)}$ Hz=0.5 Hz.

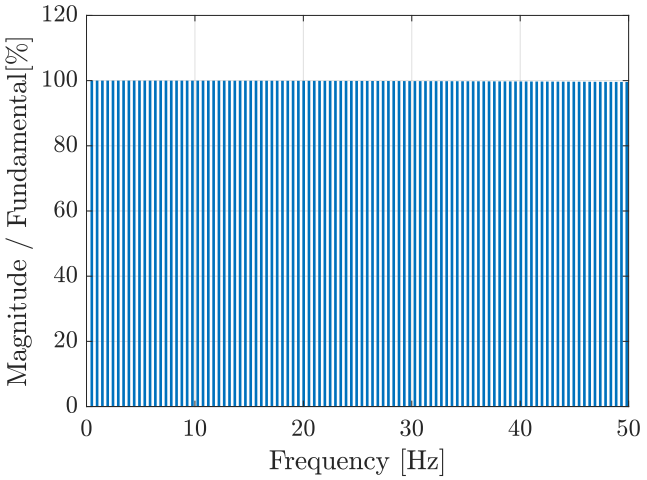

Figure 4.9: Fourier spectrum of 11-bit PRBS with $\Delta t_s = 10^{-3}$ s.

In Figure 4.9 it can be seen that the columns in the FFT frequency spectrum are close to the same height.

Then, for the configuration of the PRBS generator, there are also some considerations that must be made. In fact, the position of the XOR feedback legs will determine the sequence generated by the PRBS. However, not all configurations produce a full length sequence, meaning some bit combinations are excluded. This is disadvantageous for a few reasons. Firstly, having a shorter sequence of numbers is equivalent to using fewer bits for the PRBS. As a result, more computational power is used than is necessary when fewer bits would have been sufficient. Secondly, excluding some numbers will, as can be seen from Equation (4.22) increase the fundamental frequency, which means that the resolution of the FFT will decrease, especially in the lower frequency range.

Therefore, it is necessary to choose XOR feedback positions that produce full length cycles of the PRBS.

In this project, it has been chosen to use 11 bit PRBS with a $\Delta t_s = 0.001$ s. This provides a fundamental frequency of 0.489 Hz. This means the PRBS will not capture frequencies lower than 0.5 Hz, but it will capture relatively high frequencies, as can be seen from Figure 4.10, which illustrates the frequency content of the resulting PRBS signal.

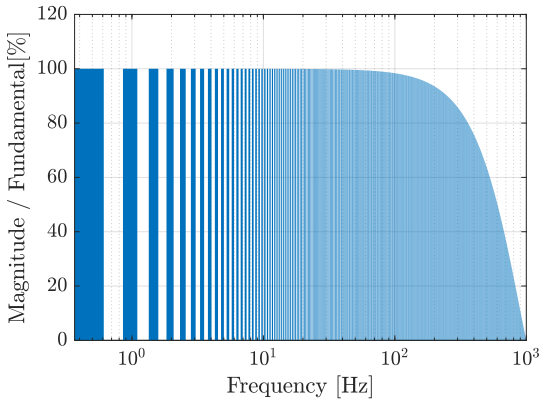

Figure 4.10: Logarithmic Fourier spectrum of PRBS signal with 11 bits and a $\Delta t_s = 0.001$ s.

In Figure 4.10, it can be seen that the magnitude stays mostly constant until around 100 Hz, where there is a significant drop in magnitude. Therefore, when applying this signal to achieve the Nyquist plot, only the lower frequency area of the graph can be obtained, since the very high frequencies are not equal in magnitude. Normally, the usable frequency band is defined as all frequencies up to -3 dB in magnitude [15]. This corresponds to around 71% in magnitude in Figure 4.10. This means that this PRBS design is usable for frequencies up to around 420 Hz. It should be underlined that, although Figure 4.10 only show the magnitudes, the FFT produces complex values, meaning the phase is also available.

However, one solution to obtain a larger spectrum for this could simply be to run several PRBS configurations to obtain different frequency spectrums of the graph, so that a complete Nyquist plot can be obtained. However, this will not be investigated in this project due to time constraints, meaning only the described configuration of 11 bits will be implemented.

4.4.3 Using PRBS to Obtain Nyquist Plot

With the battery model and 11-bit PRBS sequence constructed as previously described, this subsection will show simulation results and calculations to obtain a Nyquist plot that fits the battery. Here, no motor is present, the PRBS is simply applied from a current source through a resistor in the simulation. This is included to show the ideal case when applying PRBS on a battery, where no sources of disturbance are present.

The current and voltage graphs can be seen in Figure 4.11.

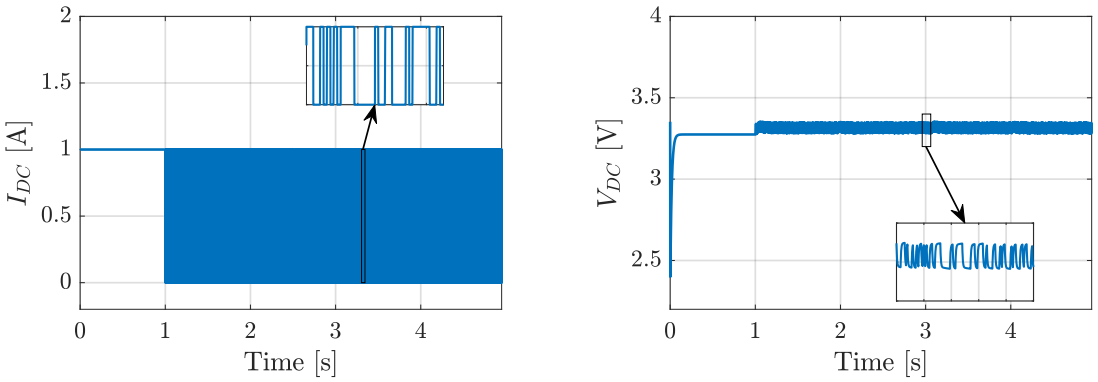

(a) (b)

Figure 4.11: Ideal battery (a) current and (b) voltage when 11-bit PRBS is injected with $\Delta t_s = 0.001$s.

This data is then treated in the "FFT analyzer", which is a feature in simulink to obtain the FFT of the signals. As explained previously, only up to 420 Hz is usable from this, so all data at higher frequencies is discarded. The data from each remaining column is then extracted to MATLAB, where the voltage is divided by the current to obtain the impedance. These values are then plotted with the theoretical Nyquist plot for the battery to obtain Figure 4.12.

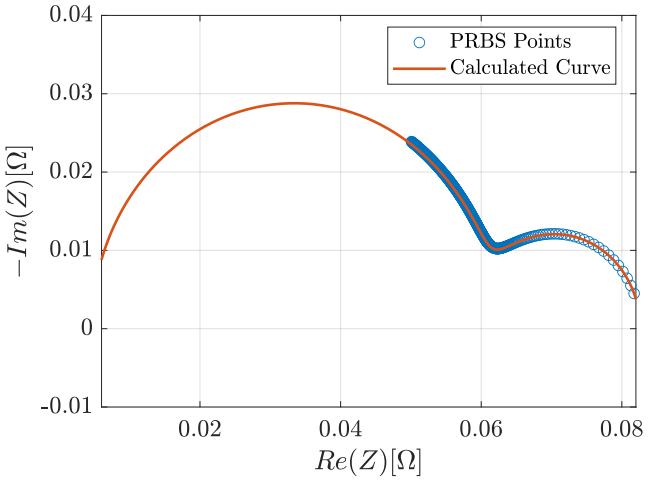

Figure 4.12: Ideal Nyquist plot generated using 11-bit PRBS with $\Delta t_s = 0.001$ s.

As can be seen from Figure 4.12, the points from the simulation lie almost exactly on top of the Nyquist plot, thus showing how the PRBS is used to obtain the Nyquist plot. Here is can be seen that the low frequency points in the right side of the curve fit perfectly on the calculated curve, while the higher frequency points start to diverge.

4.4.4 Solution for Implementation

The PRBS signal must perturb the motor operation as little as possible, while still exciting the battery enough to determine its Nyquist plot under operation. Based on

Equation (4.14), the torque of the motor is dominated by the q-axis current, especially when the motor is close to non-salient. Therefore, disturbances on i_d have a lesser effect on the torque of the motor, while still modifying the current input to the system. Injecting the PRBS on the d-axis current reference i_d^* ensures that the torque production remains unaffected during the identification process, hence minimising its impact on the motor performance. [16]

Similarly, this effect on the motor speed is expected to be negligible. It is assumed that the load torque remains constant, even if they are unpredictable for an EV, as it depends on external factors such as wind and incline of the road. In addition, as mentioned previously, the electromagnetic torque is not significantly affected, since i_q remains unchanged. Under these conditions, the rate of change of the rotor speed will also remain essentially constant, based on Equation (4.15). Consequently, it is assumed that adding the PRBS signal to the d-axis current will not cause significant disturbances to the motor operation. [16]

Also, if the inverter is assumed to be ideal, the power of the battery and the motor must be equal. Therefore, if i_d suddenly increases, it can be seen from Equation 4.23 that there is a sudden increase in power. Due to the capacitive nature of the battery, to meet this power increase, the DC current must increase similarly to the d-current of the motor.

$$P_{total} = \frac{3}{2}(v_d \cdot i_d + v_q \cdot i_q) \tag{4.23}$$

Therefore, it is chosen to inject the PRBS on the d-axis, as it is assumed that the PRBS signal will be translated through the inverter with minimal impact on the motor. This approach will be verified in the following chapters.

5. System Description & Tuning of the Controllers

In this chapter, the laboratory setup that will be used in this project is presented. Based on the parameters from the setup, controller tuning is performed and the corresponding simulation results are shown. Practical validation of the theoretical tuning is conducted in Chapter 7.

5.1 System Description

For this project, a laboratory setup has been constructed that will be used to validate the findings. As tests on a real EV would be more complex, time consuming, and hazardous, the laboratory setup consists of a PMSM with a DC motor connected at the shaft as a load. The PMSM is powered by a DC power supply using a Speedgoat PWR-TPI6020 two-level three-phase inverter for AC voltage generation. The inverter is controlled using a Speedgoat unit real-time target machine. The programming for the unit real-time target machine is done through the Speedgoat real-time Simulink blockset, which allows direct control of the machine through Simulink.

The PMSM used is the EXMEX Electric ME070AS202, which has the parameters given in Table 5.1. Some of the parameters have been measured specifically for this project, while others have been provided by the EXMEX Electric datasheet of the motor. The measurements for the parameters can be seen in Appendix A.

Table 5.1: Electrical parameters for EXMEX Electric ME070AS202.

Parameter	Value	Unit
Number of pole pairs	4	[-]
Supply Voltage	48	[Vdc]
Rated Torque	1.02	[Nm]
Rated Speed	3000	[rpm]
Rated Current	10.47	[A]
Terminal Resistance	0.25	[Ω]
Rotor Inertia	$4.58 \cdot 10^{-3}$	$[kgm^2]$
Torque constant	0.1089	$[\frac{\text{Nm}}{\text{A}}]$
L_q	1.065	[mH]
L_d	1.065	[mH]
λ_{mpm}	0.0393	[Wb]

Note here that the inertia listed is the collective inertia for both motors, as they are connected at the rotors. The PMSM is equipped with an encoder that generates 1024 pulses per rotation on 2 channels.

The battery used in the project is a Lithium-Iron-Phosphate (LiFePo4) from the com-

pany A & S of the model AS1868117. Each cell has the datasheet parameters described in Table 5.1.

Table 5.2: Electrical parameters for LiFePo4 AS1868117 [18].

Parameter	Value	Unit
Capacity	10	[Ah]
Nominal Voltage	3.2	[V]
Discharge Cut-off Voltage	2.5	[V]
Standard Dischcharge	10	[A]
Continuous Dischcharge	20	[A]
Maximum Dischcharge	30 for 10 s	[A]

Using the described cell, a battery pack has been constructed, which consists of 16 cells in series, producing a nominal voltage of 51.2 V.

The complete laboratory setup is illustrated in Figure 5.1.

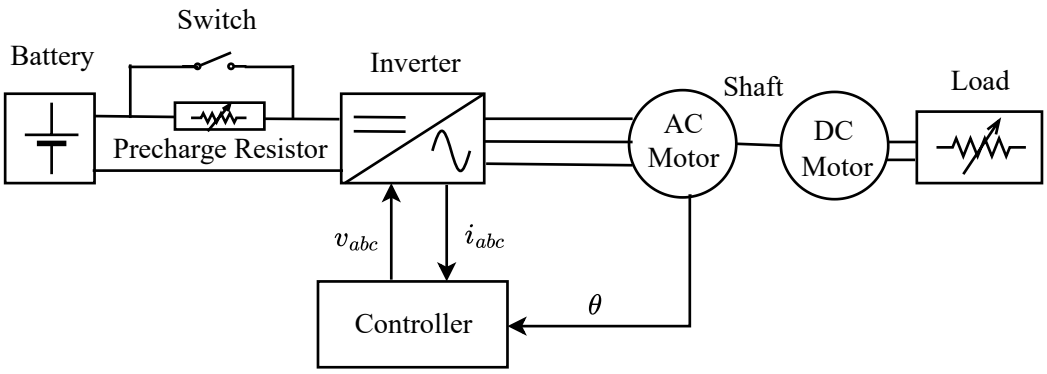

Figure 5.1: Representation of laboratory setup.

In Figure 5.1, the power supply can be either a laboratory power supply or a battery. Both will be used, as comparisons between different operations will be made. This will be explained further in Chapter 7.

5.2 Implementation of Control Structure in Simulation

This section describes the theory behind obtaining the controller gains for current and speed control. The theoretical gains will serve as a basis for tuning the controller in both the simulation environment and the laboratory.

5.2.1 Current Controller Tuning

After decoupling the i_d and i_q currents in Equation (4.18), the current open loop can be simplified as following:

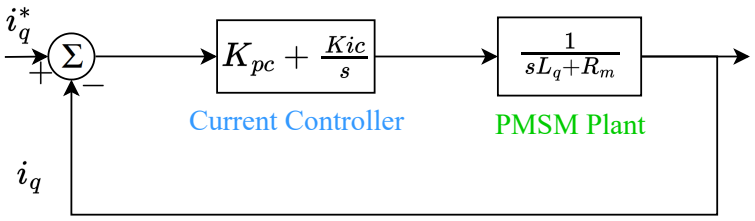

Figure 5.2: Simplified current control diagram.

which gives the following open loop transfer function:

$$G_{\mathrm{OL},\,i_q}(s) = \left(K_{pc} + \frac{K_{ic}}{s}\right)\frac{1}{L_q s + R_m} \tag{5.1}$$

Rearranging the expression in Equation 5.1, the following equivalent expression can be obtained:

$$G_{\mathrm{OL},\,i_q}(s) = \frac{s + \dfrac{K_{ic}}{K_{pc}}}{\dfrac{s}{K_{pc}}}\,\frac{\dfrac{1}{L_q}}{s + \dfrac{R_m}{L_q}} \tag{5.2}$$

As seen in Equation (5.2), the current open loop could be further simplified from a second order plant to a first order plant by making the following definition:

$$\frac{K_{ic}}{K_{pc}} = \frac{R_m}{L_q} \tag{5.3}$$

As a result, the following first order current open loop is obtained:

$$G_{\mathrm{OL},\,i_q}(s) = \frac{K_{pc}}{L_q s} \tag{5.4}$$

Assuming a standard negative unity-feedback loop, the closed-loop transfer function becomes:

$$G_{\mathrm{CL},\,i_q}(s) = \frac{G_{\mathrm{OL},\,i_q}(s)}{1 + G_{\mathrm{OL},\,i_q}(s)} = \frac{K_{pc}}{L_q s + K_{pc}} \tag{5.5}$$

By normalising the closed loop expression, the relationship between the current loop time constant τ_i and the controller and system parameters is obtained as:

$$G_{\mathrm{CL},\,i_q}(s) = \frac{1}{\frac{L_q}{K_{pc}}s + 1} = \frac{1}{\tau_i s + 1}, \quad \tau_i = \frac{L_q}{K_{pc}} \tag{5.6}$$

Knowing that the time constant τ_i is inversely related to the closed-loop bandwidth ω_{Bi} of the system through the relation:

$$\omega_{BI} = \frac{1}{\tau i} = \frac{K_{pc}}{L_q} \tag{5.7}$$

The closed loop current transfer function can be defined as a function of the desired current controller bandwidth as expressed below:

$$G_{\mathrm{CL},\,i_q}(s) = \frac{\omega_{Bi}}{s + \omega_{Bi}} \tag{5.8}$$

Therefore, the K_{pc} and K_{ic} controller gains can be tuned based on the desired current controller bandwidth. The following expressions are obtained from Equations (5.7) and (5.3), respectively:

$$\begin{aligned} K_{pc} &= \omega_{Bi} L_q \\ K_{ic} &= \omega_{Bi} R_m \end{aligned} \tag{5.9}$$

The selected bandwidth value should be fast enough to control the dynamics of the PMSM, but also slow enough so that the switching frequency is not injecting noise into the current loop. Throughout this project, the switching frequency is selected as 10 kHz in simulation environment. Therefore, the selected bandwidth is 500 Hz, given the following K_{pc} and K_{ic} gains:

Table 5.3: Theoretical K_{pc} and K_{ic} gains for the current controller.

Controller	K_{pc}	K_{ic}
Current Loop	3.35	785.4

To verify that the designed controller correctly follows the reference, a step in i_q is performed in the simulation environment, as shown in Figure 5.3. In the simulation, the inverter is present. However, this theoretical tuning was performed without considering the inverter in the plant,as shown in Figure 5.2. The inverter is excluded under the assumption that the inverter accurately produces the reference voltage. The resulting step response is shown in Figure 5.3.

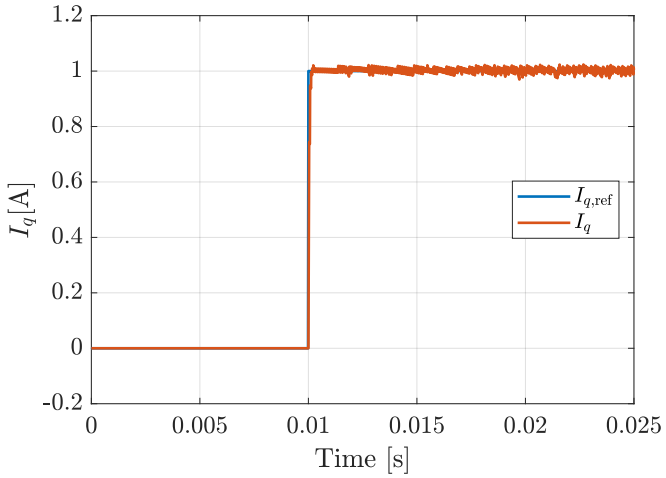

Figure 5.3: Current step in i_q in simulation environment.

Figure 5.3 shows $i_{q,ref}$ and i_q, in which i_q current is following the $i_{q,ref}$ even though there is some noise especially when step current is applied. This noise may arise due to the switching of the inverter or the absence of viscous and static friction of the motor.

Since it is assumed that the motor is non-salient, the same K_{pc} and K_{ic} controller gains can be used with the i_d current control. However, since the PRBS is injected in i_d controller gains, the controller gains must be sufficiently fast to accurately track the high-frequency PRBS. Therefore, its controller gains have been increased by a factor of 10.

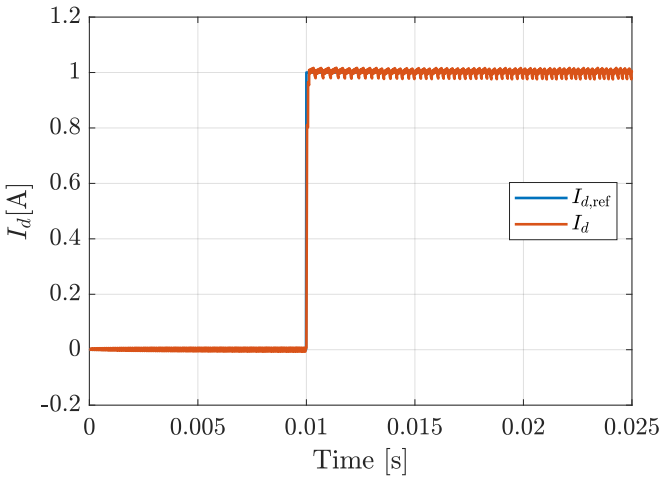

Figure 5.4: Current step in i_d in simulation environment.

Figure 5.4 shows that the step current $i_{d,ref}$ is followed by the i_d current. By increasing the gain, the error in the i_d current is minimised, where the PRBS signal will be injected. As described in Chapter 4.4.4, i_d current has no role for the torque, due to which there is minimal noise in the signal. As shown in Table 5.4, current controller gains are taken for simulation.

Table 5.4: Selected K_{pc} and K_{ic} gains for the current controller.

Controller	K_{pc}	K_{ic}
i_q	3.35	785.4
i_d	33.5	7854

5.2.2 Speed Controller Tuning

To define the plant of the speed controller, some simplifications have been made. First, the load torque is assumed to be zero while tuning speed-controller gains. This neglects the disturbance in the system, making it simpler to obtain the linearised plant. The simplified speed-control diagram is shown in Figure 5.5.

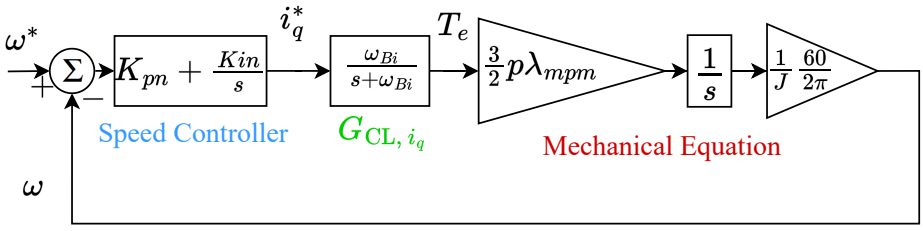

Figure 5.5: Simplified speed control diagram.

To further simplify the control structure, the constant values of the mechanical equation can be a group in one single constant, defined as:

$$K_n = \frac{3}{2}p\lambda_{mpm}\frac{1}{J}\frac{60}{2\pi} = \frac{45p\lambda_{mpm}}{J\pi} \tag{5.10}$$

Therefore, the open loop transfer function of the speed loop is:

$$G_{\mathrm{OL},\omega}(s) = \left(K_{pn} + \frac{K_{in}}{s}\right) \frac{\omega_{Bi}}{s + \omega_{Bi}} \frac{K_n}{s} \tag{5.11}$$

As shown in Equation (5.11), the open-loop speed response depends on the bandwidth of the current controller. Consequently, the outer-loop dynamics should be slower than the inner loop, so that changes in the inner loop can settle before any changes occur in the outer loop.

To ensure that the speed loop is slower than the current loop, a ratio between their bandwidths, ω_{Bi}/ω_{Bn}, is defined. This ratio determines the balance factor between the velocity and damping of the speed loop, δ. The relationship between the bandwidth ratio and δ is obtained through empirical curve-fitting analysis, extracted from the DSP User's Guide [19]:

$$\frac{\omega_{Bi}}{\omega_{Bn}} = \delta + 2.16e^{-\frac{\delta}{2.8}} - 1.86 \tag{5.12}$$

Consequently, based on the desired bandwidth ratio between the speed and current loops, δ is calculated in (5.12), and then the speed controller gains are theoretically tuned according to the following equations [19]:

$$\begin{aligned} K_{ip,n} &= \frac{\omega_{Bi}}{\delta^2} \\ K_{pn} &= \frac{K_{ip,n}\delta}{K_n} \\ K_{in} &= K_{pn}K_{ip,n} \end{aligned} \tag{5.13}$$

The selected bandwidth ratio between the speed and current controllers is 20, meaning that the speed-controller bandwidth is 20 times slower than the current loop. This ratio of 20 is a rule of thumb used in control. Therefore, the resulting speed-controller gains are:

Table 5.5: Selected K_{pn} and K_{in} gains for the speed controller.

Controller	K_{pn}	K_{in}
Speed Loop	1.67	13.20

In this project, the PMSM is started with a ramp in the speed control. Therefore, the speed controller gains are verified with a ramp as shown in Figure 5.6.

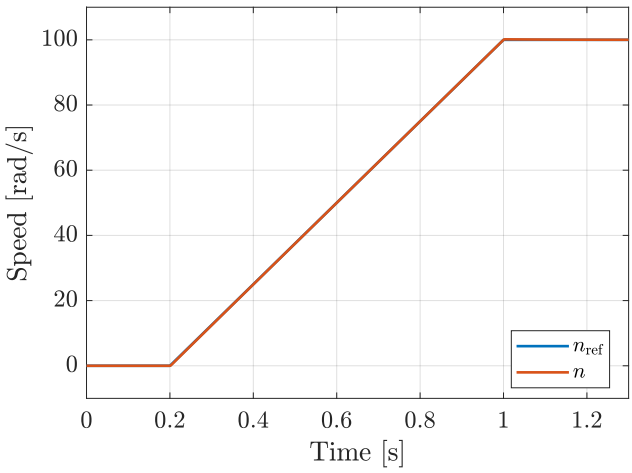

Figure 5.6: Speed ramp in simulation environment.

The Figure 5.6 shows that the speed of motor (n) is following the reference speed
545 (n_{ref}). This shows that the speed loop is working sufficiently.

6. Simulation Results

In this chapter, simulation results of the different cases are presented and analysed. For this, a model has been constructed that includes the PMSM, the inverter and the battery, as well as the PRBS sequence. All case studies are done considering load torque as zero. However, a viscous friction is inserted with a coefficient of 0.00046 $\mathrm{kg} \cdot \mathrm{m}^2$. For the 4-bit PRBS, both stationary and rotating operating conditions are considered. In contrast, the 11-bit PRBS requires significantly more computation, and as such it was not possible to run within a reasonable time frame, so its analysis has been omitted. However, since the only change from 4-bit PRBS and 11-bit PRBS is the length of the sequence, it is assumed that if 4-bit works in simulation, so should 11-bit.

6.1 Analysis of 4-Bit PRBS Generation Under Stationary Motor Conditions

For this case, the reference current i_q^* is set to zero. Therefore, the speed loop is not activated and, based on Equation (4.19), the motor will not move. The aim is to observe the PRBS in the DC current and voltage without the influence of the speed controller. The i_d and I_{DC} currents when the 4-bit PRBS is applied are shown in Figure 6.1b.

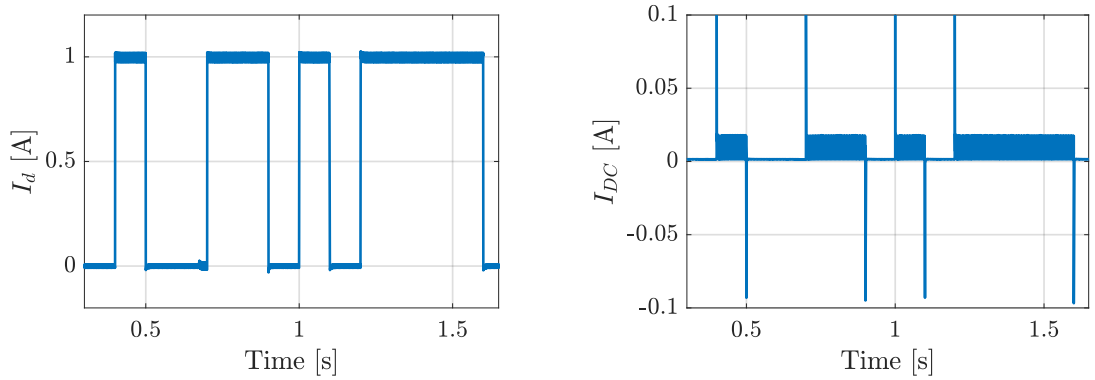

(a) (b)

Figure 6.1: (a) i_d and (b) I_{DC} during 4-bit scenario with $\Delta t = 0.1$ s.

As seen in Figure 6.1a, the PRBS can be observed with the correct amplitude in the i_d current. However, when it is injected into the DC current through the inverter, its amplitude is reduced by a factor of approximately fifty. This reduction is caused by the differences in voltage on each side of the inverter. Moreover, it can be observed that there is a large harmonic content in the DC current due to switching noise.

Since the motor is not rotating, i_d is the dominant current. Therefore, the PRBS

behaviour is not disturbed. In the following cases, this dominance of i_d will be further analysed and, if necessary, the PRBS amplitude will be increased. The presence of PRBS can be seen in the DC voltage, as illustrated in Figure 6.2, but due to the low amplitude of the current, the voltage response is also small.

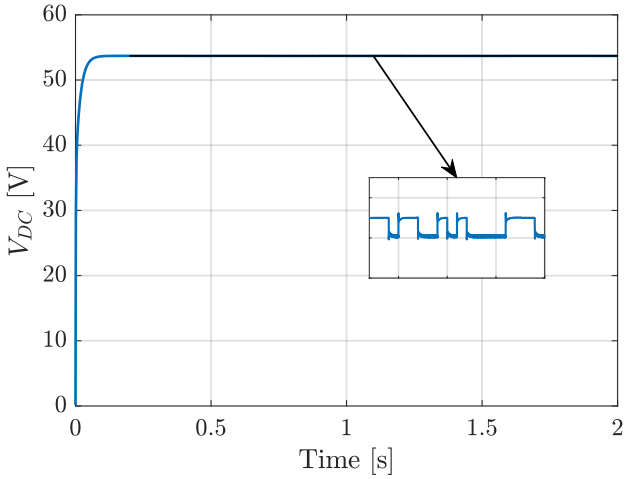

Figure 6.2: V_{DC} during 4-bit scenario with $\Delta t = 0.1$ s.

The frequency content of the 4-bit PRBS with a sample time of 0.1 seconds is shown in Figure 6.3.

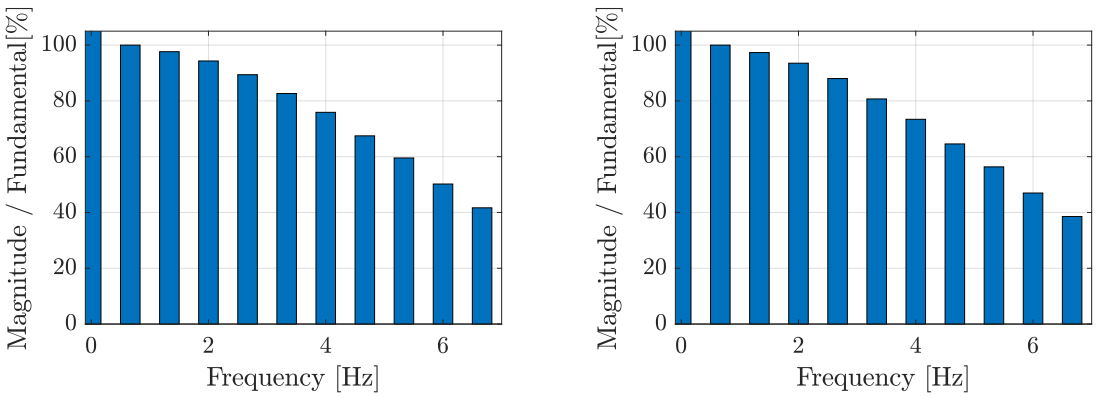

Figure 6.3: Bar chart of FFT magnitudes when 4-bit PRBS is injected with $\Delta t = 0.1$ s : (a) Current and (b) Voltage.

As illustrated in Figure 6.3, the usable frequency spectrum of both current and voltage is very limited due to the shortness of the PRBS sequence and the large sample time. Consequently, the PRBS points obtained lie only in the low-frequency range, as shown in Figure 6.4, which limits the identification of the higher-frequency area of the Nyquist plot.

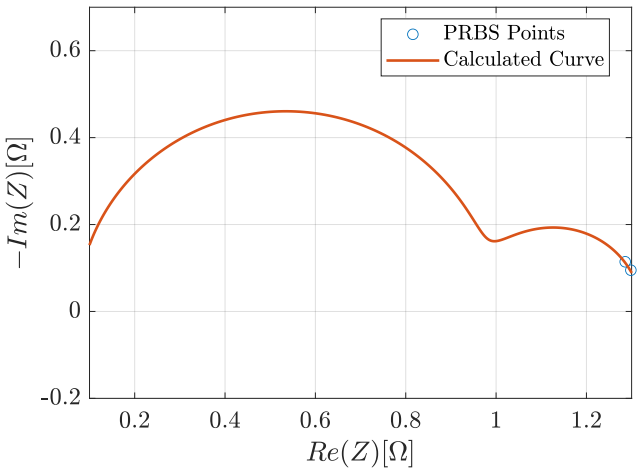

Figure 6.4: Nyquist plot obtained from 4-bit PRBS with $\Delta t = 0.1$ s.

To increase the estimated frequency range, the PRBS sample time was reduced to 0.001 seconds. Consequently, the frequency content of voltage and current has significantly increased, as illustrated in Figure 6.5.

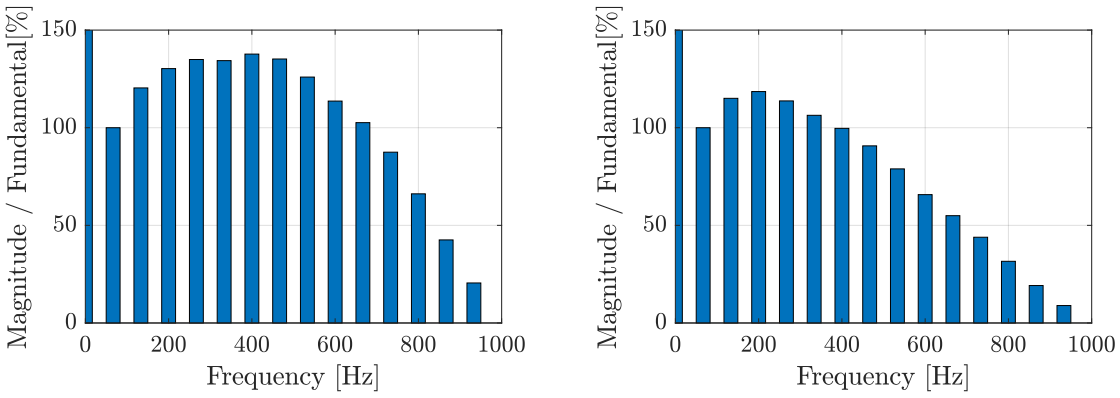

Figure 6.5: Bar chart of FFT magnitudes when 4-bit PRBS is injected with $\Delta t = 0.001$ s : (a) Current and (b) Voltage.

As a result, the PRBS points now fit the Nyquist plot even at higher frequencies, as illustrated in Figure 6.6.

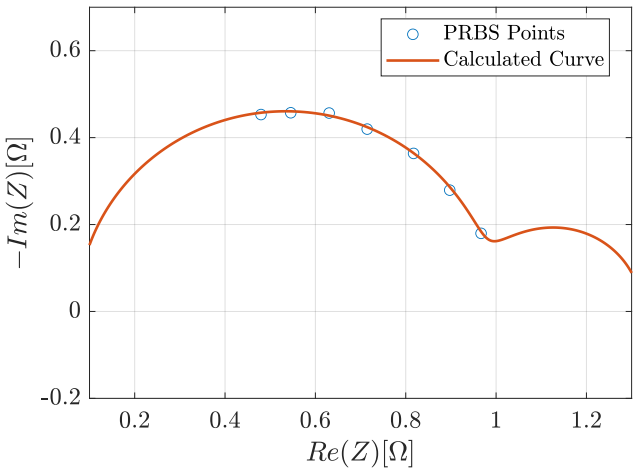

Figure 6.6: Nyquist plot obtained from 4-bit PRBS with $\Delta t = 0.001$ s.

With the reduced sample time, the PRBS excites a much wider frequency band, improving the accuracy of the identified segment of the Nyquist plot.

6.2 Analysis of 4-Bit PRBS Generation Under Motor Operating Conditions

The same procedure described in Section 6.1 will be used to analyse the 4-bit PRBS while the motor is running. For that, the output of the speed loop is the reference for i_q^* instead of a zero constant as it was in Section 6.1. This allows the motor to rotate while the PRBS is applied. The resulting i_d and I_{DC} currents are shown in Figure 6.7.

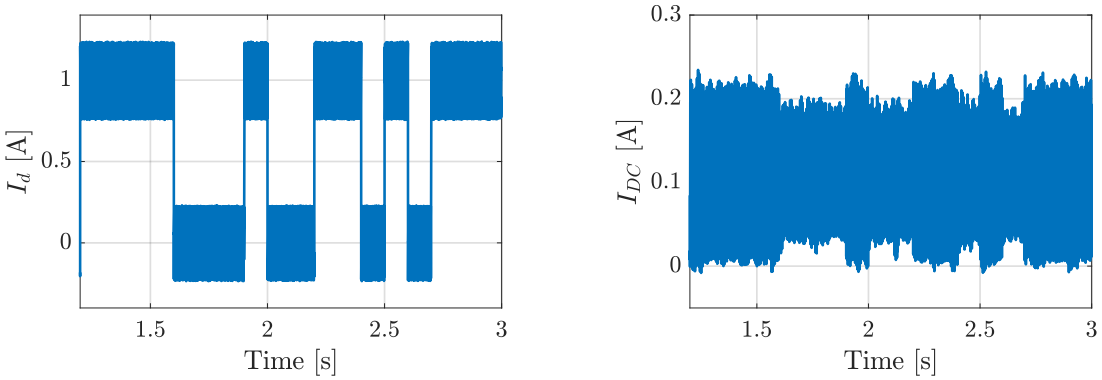

(a) (b)

Figure 6.7: (a) i_d and (b) I_{DC} during 4-bit scenario with $\Delta t = 0.1$ s and a gain of 1, while motor is running.

As seen in Figure 6.7a, the PRBS is applied correctly in the i_d current, indicating that the current controller is tuned properly to follow the PRBS pattern. However, it is difficult to clearly see the same pattern in the DC current, as shown in Figure 6.7b. When i_q is present, which has a significantly greater amplitude than the i_d current, the fast variations injected in i_d become less visible in the DC current. However, this

distortion of the PRBS does not result in a less accurate Nyquist plot compared to the previous case, as seen in Figure 6.4.

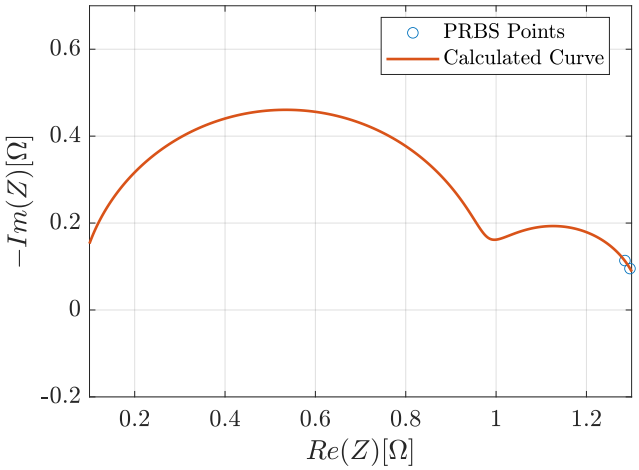

Figure 6.8: Nyquist plot obtained using a 4-bit PRBS with a gain of 1 while the motor is running, with $\Delta t = 0.1$ s.

To increase the dominance of the i_d current, a gain of 2 is inserted in the PRBS, resulting in the i_d and I_{DC} currents shown in Figure 6.9.

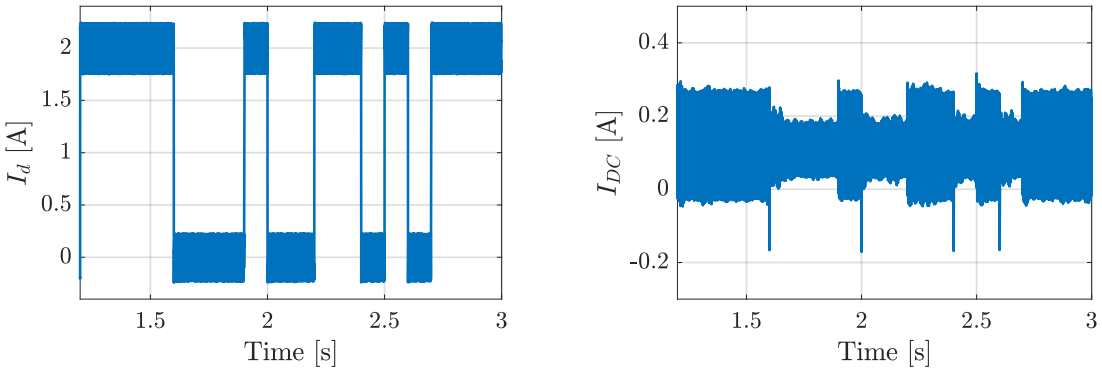

Figure 6.9: (a) i_d and (b) I_{DC} during 4-bit scenario with $\Delta t = 0.1$ s and a gain of 2, while motor is running.

In Figure 6.9b, the PRBS pattern is more visible when its amplitude is increased, which leads to the Nyquist plot shown in Figure 6.10, which is very similar to Figure 6.8.

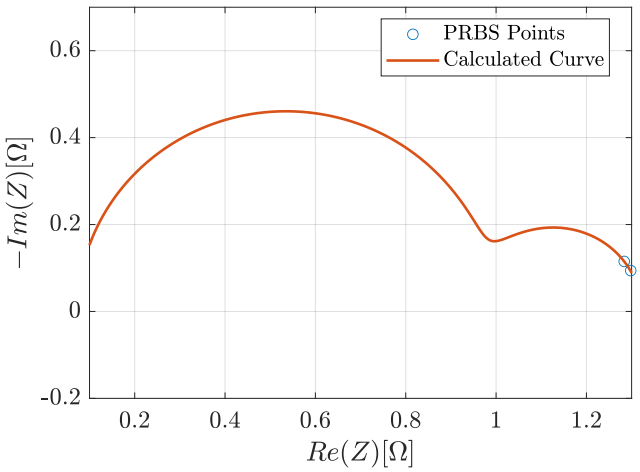

Figure 6.10: Nyquist plot obtained using a 4-bit PRBS with a gain of 2 while the motor is running, with $\Delta t = 0.1$ s.

To increase the frequency range, the sample time is reduced to 0.001 seconds, keeping the gain of 2, resulting in the i_d and I_{DC} as shown Figure 6.11.

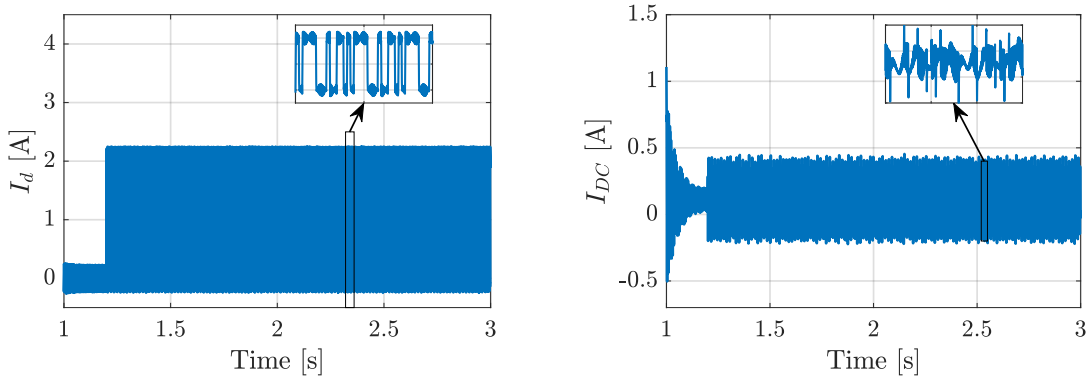

(a) (b)

Figure 6.11: (a) i_d and (b) I_{DC} during 4-bit scenario with $\Delta t = 0.001$ s and a gain of 2, while motor is running.

In Figure 6.11, it can be seen that lowering Δt_s still results in distortion in the DC current as in Figure 6.9 where Δt_s is larger. Similarly, when considering the frequency content shown in Figure 6.12, it can be seen that the low order harmonics are still clearly present and they are not affected by high frequency harmonics.

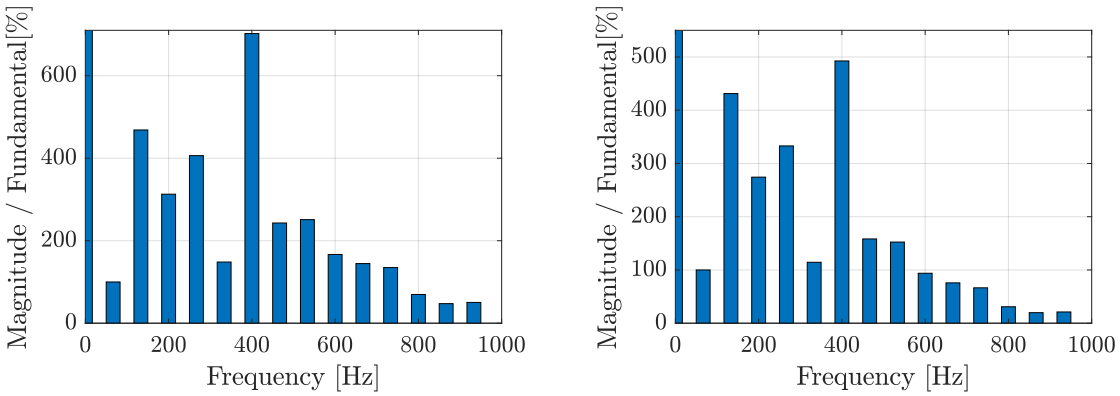

Figure 6.12: Bar chart of FFT magnitudes when 4-bit PRBS is injected, while the motor is running with $\Delta t = 0.001$ s : (a) Current and (b) Voltage.

Constructing the Nyquist plot from the data shown in Figure 6.12 yields Figure 6.13.

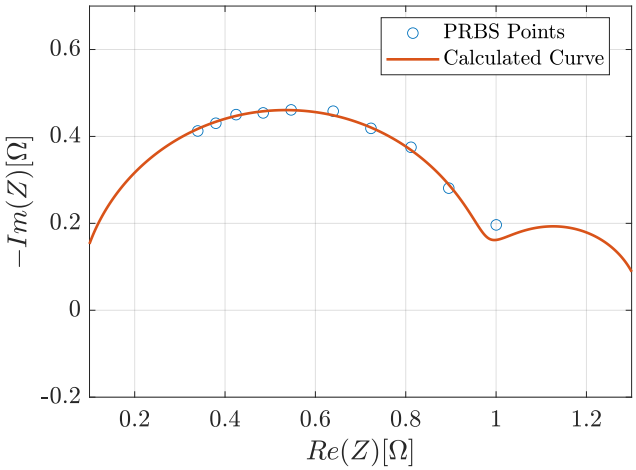

Figure 6.13: Nyquist plot obtained using a 4-bit PRBS with a gain of 2 while the motor is running, with $\Delta t = 0.001$ s.

From Figure 6.13, it can be seen, that although the PRBS signal is distorted on the DC current, the resulting Nyquist plot closely match the calculated curve, suggesting that the method works despite the distortion. This also shows, that it is not a problem when the magnitude of the harmonics are larger than the fundamental, as can be seen in Figure 6.12, since the voltage will respond correspondingly.

Based on the simulations, it has been shown that, theoretically, it is possible to obtain the Nyquist plot of a battery by applying 4-bit PRBS through the inverter. The PRBS sequence was shown to function with a step time of 0.1 s and 0.001 s, obtaining different areas of the Nyquist plot. It was that by applying the i_q current in the system, the I_{DC} current present more distortions. However, since the nature of these distortions only increase the low order harmonics in magnitude, this does not affect the Nyquist plot. It was also found that increasing the magnitude of the PRBS improves the visibility of the PRBS in I_{DC}. However, the findings in this chapter are entirely theoretical, and the model must be validated in the laboratory for the findings to be verified.

7. Laboratory Results

In this chapter, experimental validation of the findings from the previous chapter will be presented. This includes an explanation of the laboratory procedure as well as data analysis and a comparison with simulation data. As previously explained, a DC motor is connected to the PMSM, in this setup it is connected to a variable resistor that has been set to 6 Ω.

7.1 Implementation on Speedgoat Hardware Platform

To implement the control structure in lab, it was first necessary to develop a program that can run on the hardware described in Section 5.1. For this, a discrete Real-time program was developed in simulink using the Speedgoat blockset. The fundamental step size for this program was chosen as 10^{-4} s, as it was found that this was the lowest possible for the hardware to run. Likewise, the sampling rate for the measurements was chosen to be 10 kHz, as this value must be an integer multiple of the fundamental step size.

The inverter module is equipped with current measurements and input ports for an encoder, hence all necessary measurements for the control structure are taken directly from the inverter. The output from the program comes through a PWM generator block that takes the abc voltage reference and generates sinusoidal PWM based on a triangular carrier wave. The frequency of the triangular carrier was chosen at 10 kHz, yielding the same switching frequency for the inverter. A higher switching frequency was desired in order to lessen the effect of switching noise in the system, but this was not possible due to the fundamental step size of the program.

7.2 Implementation of Control Structure

This section will describe the implementation and validation process for the motor control. The control structure explained in Chapter 4 with the controllers designed in Chapter 5 was implemented and will be commented upon in this section. For this part, the battery was not implemented. Instead, a DC power supply was connected, which applied 42 V to the DC terminals of the inverter.

7.2.1 Current Loop Implementation

For the current loop, first a step is applied on the i_q reference, while the i_d reference is maintained at zero, and the response is recorded. This is shown in the Figure 7.1.

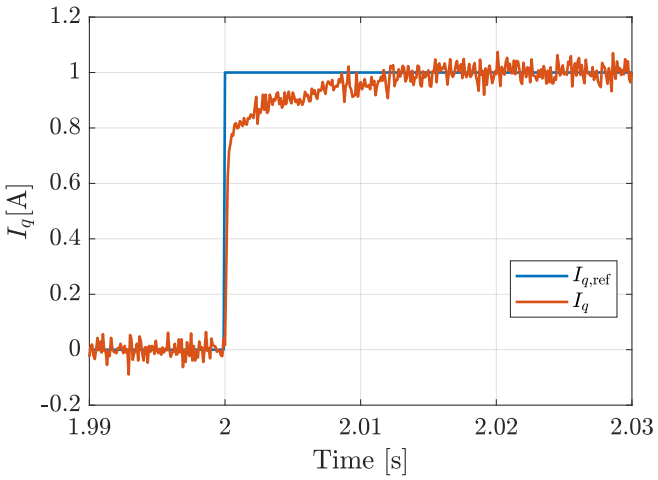

Figure 7.1: Current step in i_q.

In Figure 7.1, it can be seen that the q-axis current reaches steady state within 0.015 seconds. However, there is a significant amount of noise present that might be caused by switching or EMI from the surroundings. It could also be caused by the relatively low sampling time for the encoder, as a poor angle measurement would cause inaccurate determination of the SRF currents. Likewise, the encoder used only had 1024 pulses per revolution, which is relatively low and may therefore lead to inaccurate determination of the SRF currents. Using a more advanced encoder might mitigate the noise issue. The response time of this was deemed sufficient for the purposes of this project.

For the i_d controller, the same procedure was followed as for the i_q controller. A step is applied on the i_d reference, while the i_q reference was kept at zero. The response to the step can be seen in the Figure 7.2.

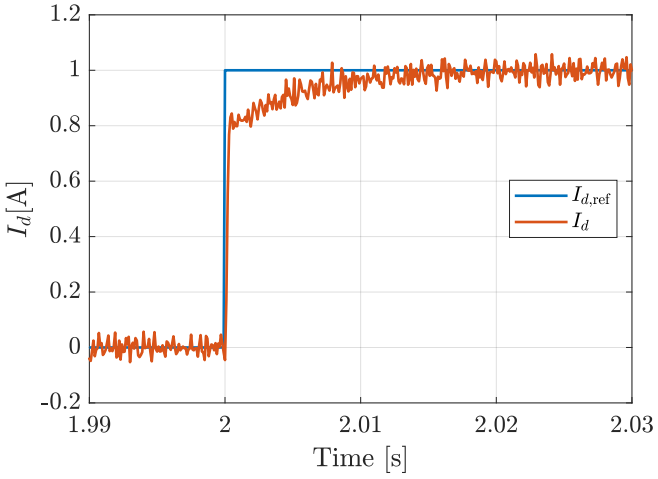

Figure 7.2: Current step in i_d.

In figure 7.2, it can be seen that i_d reaches steady state in 0.017 seconds. It can also be seen that the presence of noise is lowered for this step compared with the q-

current step. This is because the d-current step does not produce torque in the motor, resulting in no movement. This supports the idea that poor angle measurements has an influence on the amount of noise in the system. Moreover, the d-current controller has different gains than the q-current controller, which makes their behaviour slightly different.

7.2.2 Speed Loop Implementation

With the current loops verified, the speed loop were also be implemented. The same control structure and controllers described in Chapters 4 and 5 were used, with the reference ramped up to 100 $\frac{\text{rad}}{\text{s}}$ and then kept constant. The resulting response can be seen in Figure 7.3.

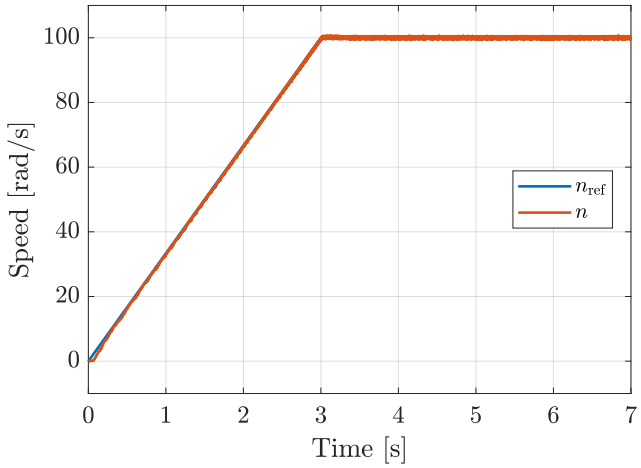

Figure 7.3: Speed ramp.

In Figure 7.3, it can be seen that the speed response follows the reference closely, but with some ripple. This ripple may be caused by fluctuations in the q-axis current, which leads to torque oscillations and, consequently, speed ripple. Based on the response of the currents as well as on the speed, it can be seen that the modelled setup behaves in accordance with reality, although the presence of noise in the physical system is a significant deviation between the two.

7.3 Inspection of Currents

It is also relevant to consider the currents when performing these tests. To avoid repetition, as the behaviour is similar across all the tests, this section will present the currents for the scenario of no PRBS being injected, as well as when the 4-bit PRBS is injected. Both scenarios have the speed loop included. The abc frame currents when no PRBS is injected are shown in Figure 7.4.

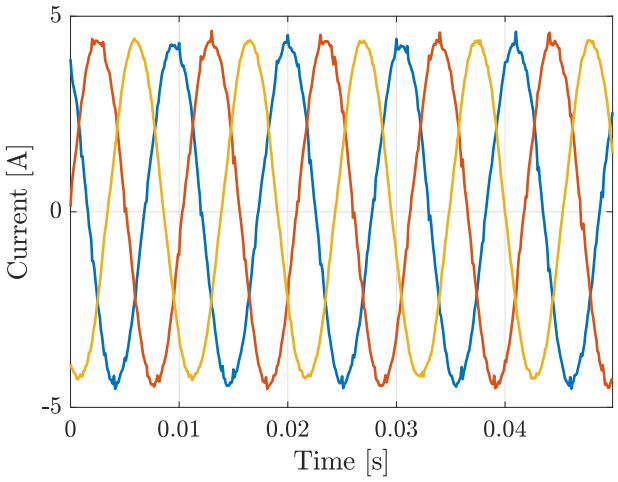

Figure 7.4: i_{abc} when no PRBS is injected.

In Figure 7.4, it can be seen that when the motor is running without PRBS injection, the currents are sinusoidal, suggesting that the system is operating as intended.

The abc frame currents when no PRBS is being injected are shown in Figure 7.5.

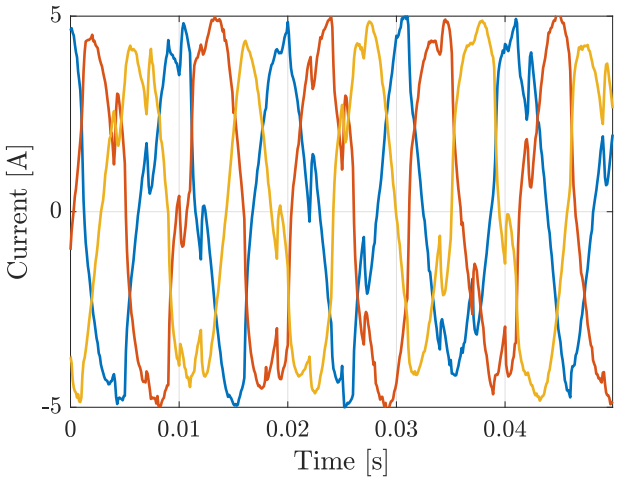

Figure 7.5: i_{abc} when 4-bit PRBS is injected.

In Figure 7.5, it can be seen that the inclusion of PRBS is the system induces distortion on the current. This is to be expected, as the rapid changes in i_d will cause rapid changes in the current.

7.4 Implementation of PRBS in Laboratory Environment

Since it was shown that the developed control structure performs adequately, it is possible to implement PRBS on the d-axis current. This section will describe the procedure used, present the results and draw conclusions. Several different implementations of PRBS is performed, both an 11-bit and a 4-bit sequence will be implemented, to see the difference between the two. Similarly to Chapter 6, these two sequences will be

implemented in two different scenarios, one with 0 speed reference and one where the motor is running. These different scenarios are chosen to investigate the significance the q current has on the quality of the PRBS signal on the DC side of the inverter.

Due to the presence of noise in the system and saliency in the motor, it was chosen to slow down the PRBS signal by lowering the step size of every bit from 0.001 s to 0.1 s. This greatly shifts the spectrum of frequencies for which the PRBS can be used to investigate the battery. Despite this, the measurements should still be valid, although not usable for the high frequency behaviour, when parametrising a battery.

7.4.1 Analysis of 4-Bit PRBS Generation Under Stationary Motor Conditions

For this test, the speed reference, and thereby the q-current reference is set to zero, while the 4-bit PRBS signal is applied on the d-current reference. The resulting waveform on the DC current can be seen in Figure 7.6.

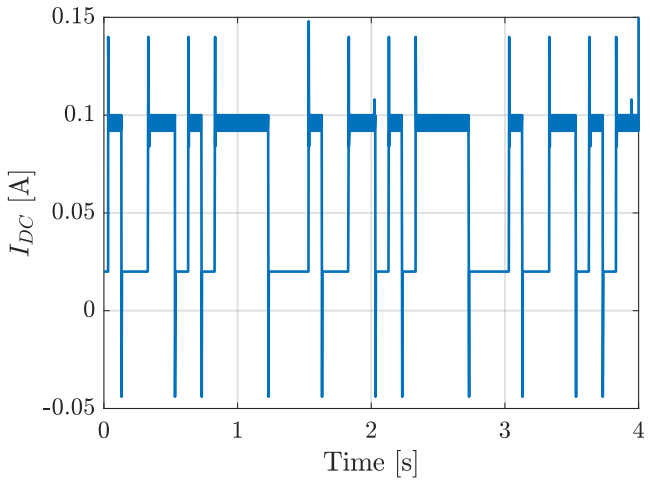

Figure 7.6: I_{DC} when 4-bit PRBS is injected.

In Figure 7.6, it can clearly be seen that the PRBS signal is present, but due to the behaviour of the PI controller as well as the inductive behaviour of the motor, the transitions from low to high are not instantaneous. However, the response is deemed satisfactory, as it closely resembles simulation.

The voltage response from the PRBS signal can be seen in Figure 7.7.

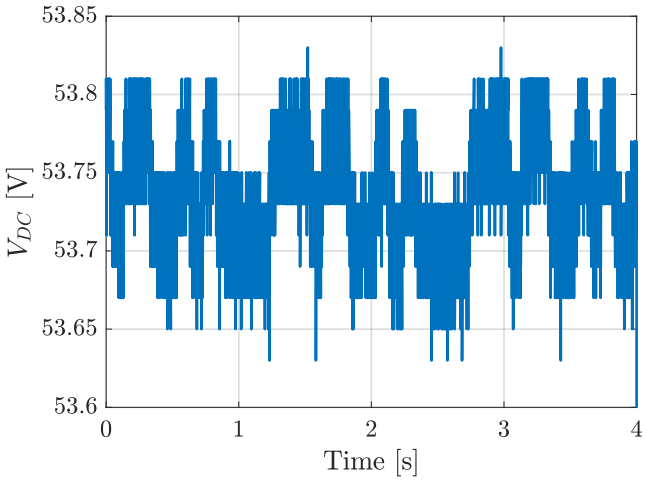

Figure 7.7: V_{DC} voltage when 4-bit PRBS is injected.

In Figure 7.7, it can be seen that there is a greater presence of noise, although it can clearly be seen that the voltage responds to the PRBS signal on the current, as expected.

FFT is then performed on both the voltage and the current in the interval of 1 period of the PRBS, yielding the two bar charts shown in Figure 7.8.

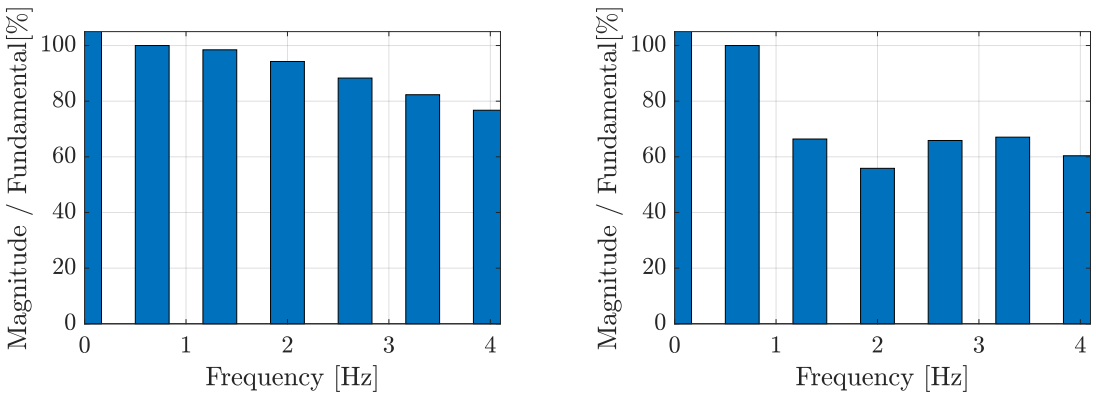

Figure 7.8: Bar chart of FFT magnitudes when 4-bit PRBS is injected. (a) Current and (b) Voltage.

Using Ohm's law, the impedance at every frequency is then calculated. Figure 7.9 shows the resulting Nyquist plot from this test.

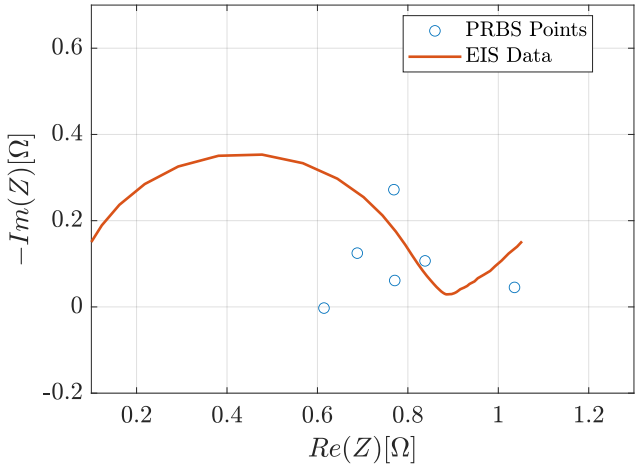

Figure 7.9: Nyquist plot obtained when 4-bit PRBS is injected.

As can be seen in Figure 7.9, the data points obtained from the 4-bit PRBS show the general tendency, but due to noises in the system, these points have a large spread from each other, and lie on both sides of the expected curve.

7.4.2 Analysis of 11-Bit PRBS Generation Under Stationary Motor Conditions

For the 11-bit PRBS sequence, the procedure is identical to the one described when implementing the 4-bit PRBS. For the 11-bit PRBS, because the sequence is very long and because the PRBS has been slowed down, the fundamental frequency is 0.005 Hz. Therefore this sequence will, as with the 4-bit PRBS only describe the low frequency behaviour of the battery. However, due to the length of the sequence, the 11-bit PRBS scenario will produce a much wider frequency spectrum, yielding a higher resolution in the Nyquist plot. The current from the 11-bit PRBS sequence can be seen in Figure 7.10.

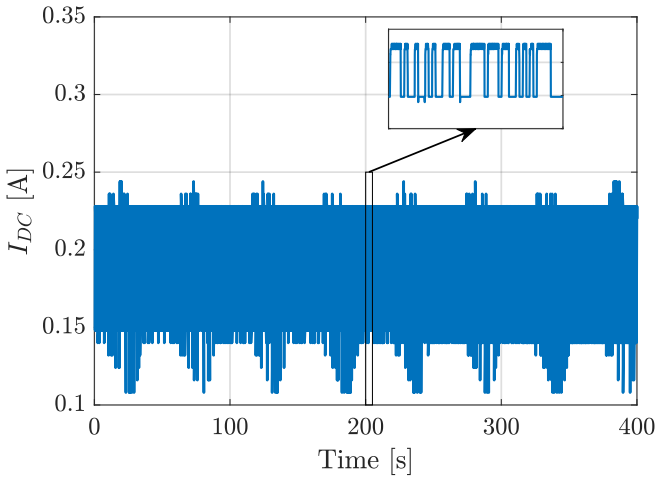

Figure 7.10: I_{DC} when 11-bit PRBS is injected.

Although not immediately visible due to the time scale of the figure, the PRBS signal

is present on the current, similarly to Figure 7.6. It can be seen from the Figure 7.6 that there are some low frequency spikes that occur at approximately every 30 seconds. This phenomenon likely has influence on the results from this test, especially in the very low frequencies. The voltage response produced by this current can be seen in Figure 7.11.

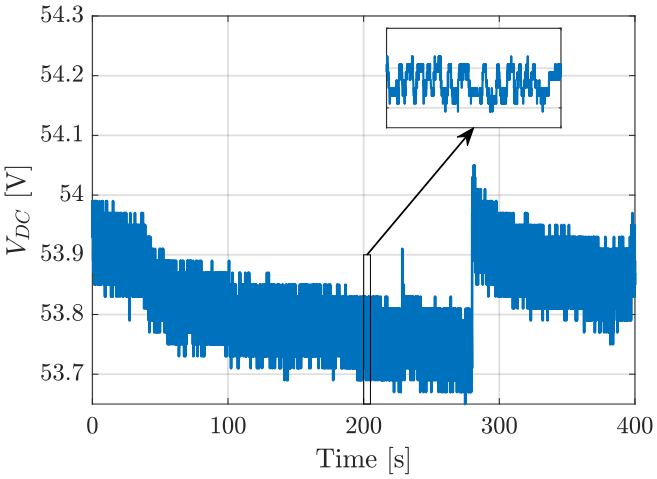

Figure 7.11: V_{DC} when 11-bit PRBS is injected.

In Figure 7.11, the PRBS signal is not obvious from the figure due to the time scale, but could be seen on a shorter time scale. From Figure 7.11, even slower dynamics are present, as can be seen at approximately 280 s, where the voltage suddenly jumps. However, this behaviour is unlikely to affect the resulting Nyquist plot, as it is slower than the fundamental frequency of the PRBS and therefore lies outside the considered frequency spectrum. Performing FFT on the voltage and current just presented yields Figure 7.12.

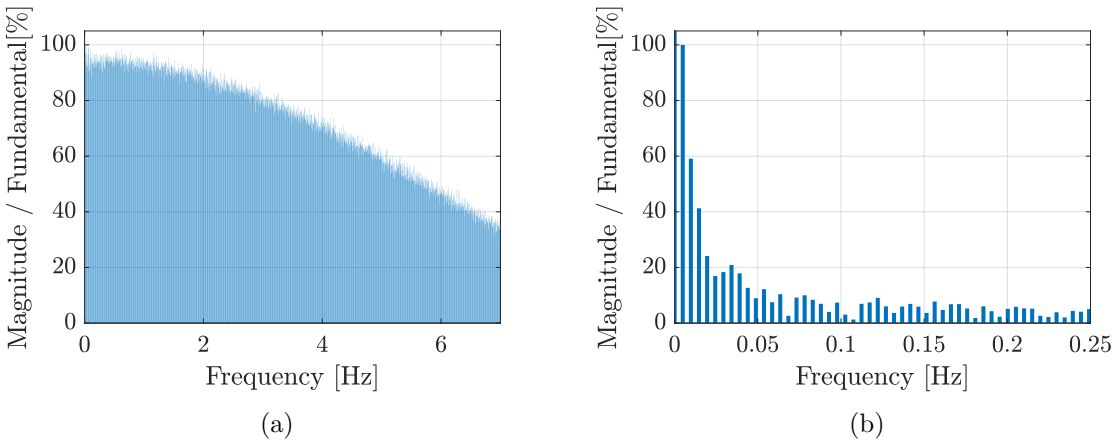

Figure 7.12: Bar chart of FFT magnitudes when 11-bit PRBS is injected. (a) Current and (b) Voltage.

As can be seen from Figure 7.12, the resolution of the FFT is several orders of magnitude greater than for the 4-bit PRBS. It is evident that the battery voltage reaction is the greatest for the very low frequency PRBS content. The spectrum of frequen-

cies that can be used is from the fundamental until the current curve reached -3 dB dropoff, which is at approximately 4 Hz. Although the FFT for the current may appear noise free, it still contains noise. Every frequency step varies significantly from its neighbours, which is a significant diversion from the ideal scenario. For this reason, the resulting Nyquist plot will scatter greatly, as can be seen from Figure 7.13.

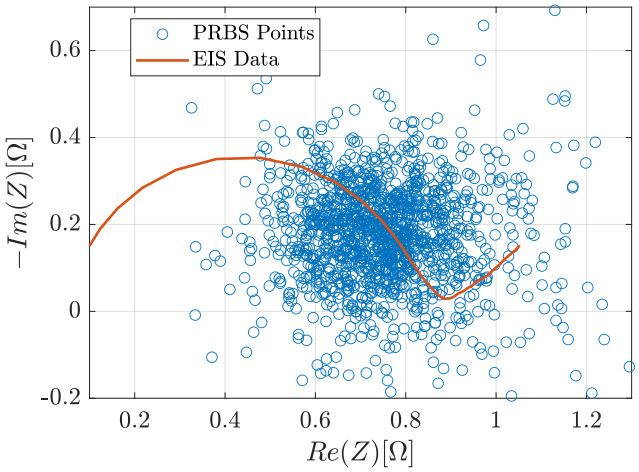

Figure 7.13: Raw Nyquist plot obtained when 11-bit PRBS is injected.

To mitigate this, it has been chosen to take the mean value for every 30 points under the assumption that their divergence from the actual curve is normally distributed. This is possible due to the very high resolution of the FFT. Doing this yields Figure 7.14.

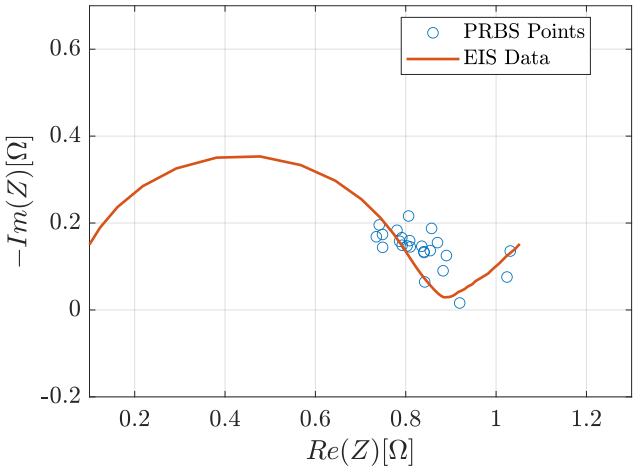

Figure 7.14: Filtered Nyquist plot obtained when 11-bit PRBS is injected.

In Figure 7.14, it can be seen that especially the very low frequency points fit the curve closely, while the higher frequency points diverge much more from the curve. How much this diverges from the real curve cannot be said however, since the specific data used here will likely vary from the actual battery used. This is due to the fact that the cell used is not new, but has been kept in storage for multiple years, meaning it will undoubtedly have some effect from calender ageing. To underline this point, the

laboratory battery has additional resistances in the form of the connectors between the cells, which are not considered for the red curve. Despite all of this, the produced Nyquist plot clearly resemble the behaviour of the battery.

7.4.3 Analysis of 4-Bit PRBS Generation Under Motor Operating Conditions

In this scenario, the speed loop operates as described in Chapter 4, with the PRBS activated after 5 seconds. This yielded the speed response shown in Figure 7.15.

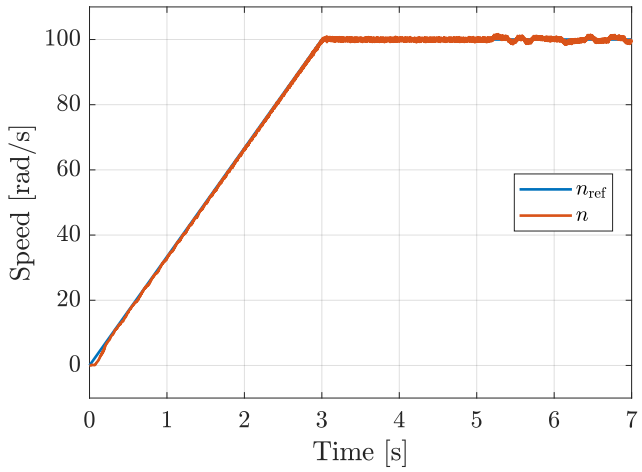

Figure 7.15: Speed performance when 4-bit PRBS is injected.

In Figure 7.15, it can be seen that the PRBS signal induces a disturbance in the speed, but the speed loop is robust enough to not become unstable.

The DC current resulting from the PRBS can be seen in Figure 7.16.

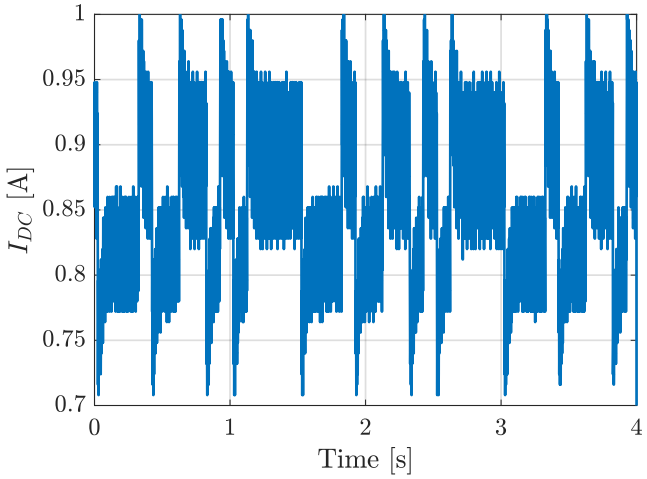

Figure 7.16: i_{DC} current when 4-bit PRBS is injected while the motor is running.

From Figure 7.16, it can be seen that the PRBS signal is also present, although with some transients when going between high and low states. Apart from these transients,

it can also be seen that there is significant high frequency noise present in the system which is much greater than in the stationary scenario.

The resulting voltage response can be seen in Figure 7.17

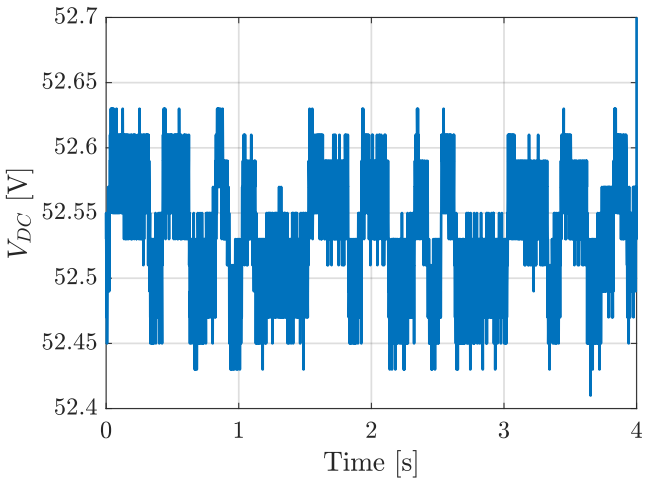

Figure 7.17: V_{0DC} when 4-bit PRBS is injected while the motor is running.

In Figure 7.17, it can be seen that the signal is affected by noise. Although the current response is worse in this case, the voltage response remains very similar to that shown in Figure 7.7. Performing FFT on the DC current and DC voltage yields Figure 7.18

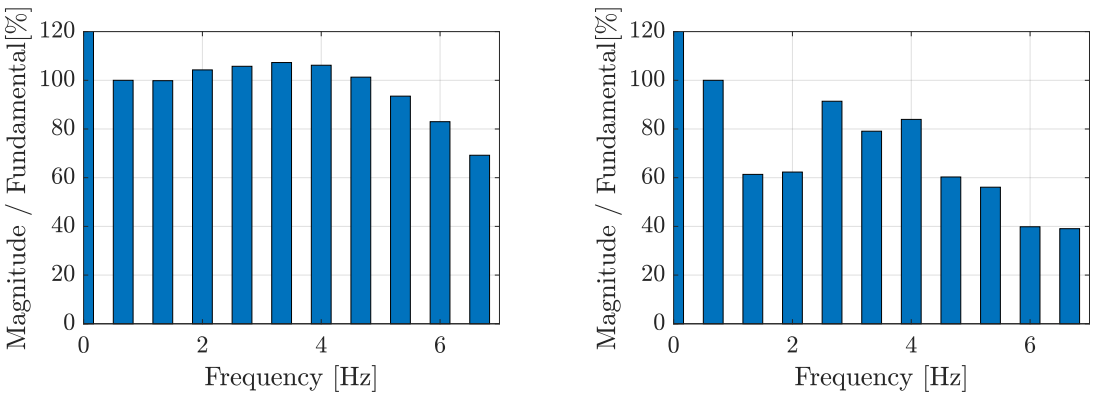

Figure 7.18: Bar chart of FFT magnitudes when 4-bit PRBS is injected, while the motor is running: (a) Current and (b) Voltage.

In Figure 7.18, it can be seen, that due to the transients just mentioned, the magnitudes of the third to seventh harmonics in the current are actually greater than the fundamental. However, the same behaviour can be seen on the voltage, meaning this phenomenon might not invalidate the results obtained. Constructing the Nyquist plot based on the FFT data yields Figure 7.19.

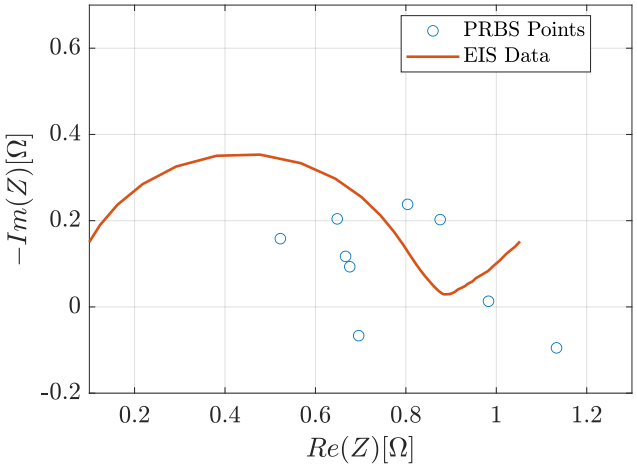

Figure 7.19: Nyquist plot obtained when 4-bit PRBS is injected, while the motor is running.

In Figure 7.19, it is obvious that some of the points are invalid. The points from the first and second harmonic are positive, which is inconsistent with the battery's predominantly capacitive behaviour. However, for the rest of the points, a curving behaviour between the points is noticeable. These points might be on the real curve for the battery, since the curve plotted from real data is for a different cell and at a different SOC, which will result in a different curve.

7.4.4 Analysis of 11-Bit PRBS Generation Under Motor Operating Conditions

In this scenario, the speed loop operates as described in Chapter 4, with the PRBS activated after 5 seconds. This yielded the speed response shown in Figure 7.20

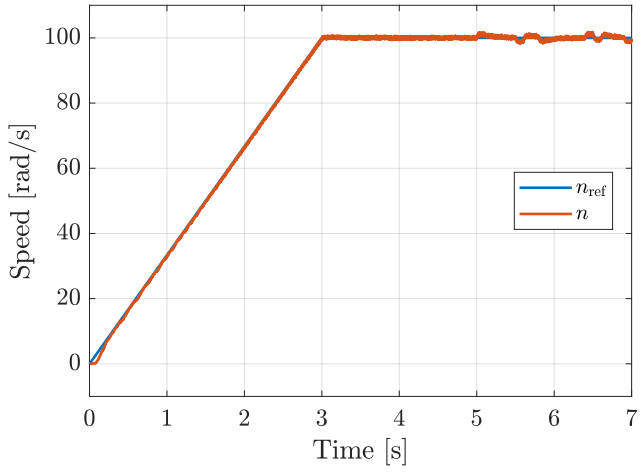

Figure 7.20: Speed performance when 11-bit PRBS is injected.

Once again, the PRBS clearly has an impact of the speed of the motor, although without making it unstable. The DC current from this test is shown in Figure 7.21.

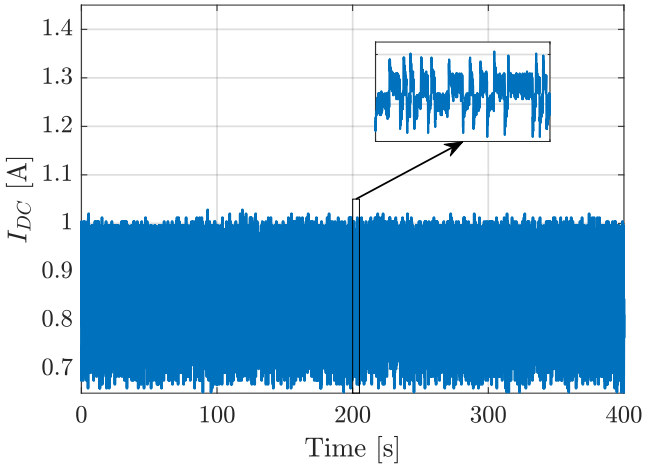

Figure 7.21: I_{DC} when 11-bit PRBS is injected, while the motor is running.

Once again, the PRBS signal is present in Figure 7.21, similarly to the 4-bit scenario, but cannot obviously be seen due to the time scale. It must be underlined that again a lot of noise is present in the system. The voltage response of this scenario can be seen in Figure 7.22.

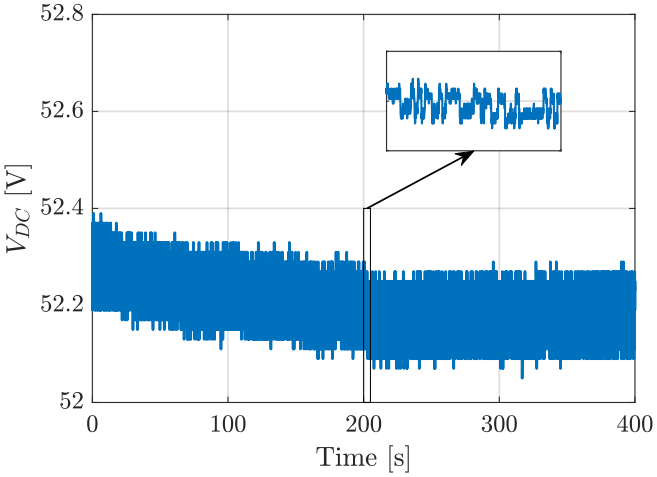

Figure 7.22: V_{DC} when 11-bit PRBS is injected, while the motor is running.

In Figure 7.18, it can be seen that the PRBS is present similarly to the 4-bit case, but with a lot of noise. Also, there is a very slow dynamic in the system, apart from the PRBS signal. Performing FFT on the current and voltage yields Figure 7.23.

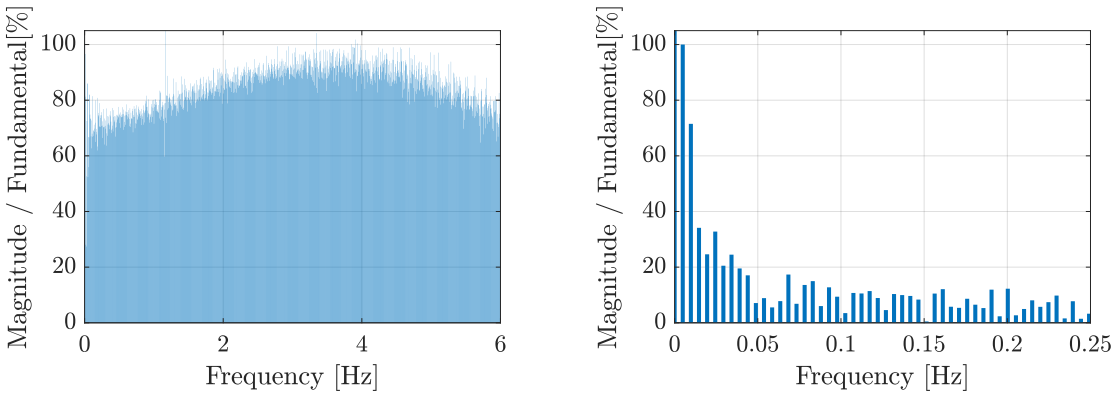

Figure 7.23: Bar chart of FFT magnitudes when 11-bit PRBS is injected, while the motor is running: (a) Current and (b) Voltage.

In Figure 7.23, it can be seen in the current magnitudes that the very low frequencies drop in magnitude, while the higher frequencies increase in magnitude, which is different from what would be expected from the PRBS signal. Constructing the Nyquist plot from this data yields Figure 7.24. Again, the mean of every 30 points has been taken in order to eliminate some of the effects of the noise.

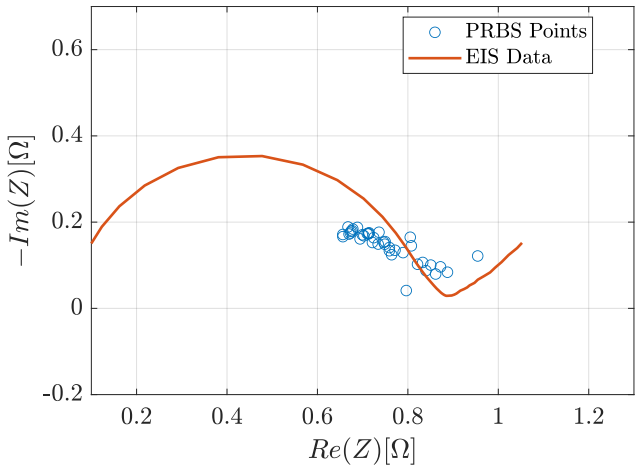

Figure 7.24: Filtered Nyquist plot obtained when 11-bit PRBS is injected, while running the motor.

In Figure 7.24, it can be seen that the tendency of the battery impedance can be seen, and as mentioned previously, the battery has aged since the curve of the EIS Data was taken, suggesting that the PRBS points may provide a more accurate representation of the current battery.

Based on the four test presented in this chapter, it can be concluded that the PRBS method effectively captures the behaviour of batteries connected to a PMSM. However, as was seen from the great spread in the data points, this method is sensitive to noise. Also, due to the limited spectrum of frequencies in the PRBS signal, the method will only give part of the EIS plot. This problem could be solved by implementing

more than one PRBS sequence, and assemble the full curve from different tests. This will then pose another problem, since the high frequency area of the Nyquist plot will require a very fast PRBS signal. This is a challenge since the motor is mostly inductive, and as such rapidly changing currents in the d-axis without distortion of the PRBS signal might be difficult to obtain. Therefore, for industrial implementations, improved filtering should be implemented and it should be considered which area of the Nyquist plot is of interest, depending on the specific use case.

8. Conclusion

The purpose of this project has been to investigate the PRBS method for obtaining the Nyquist plot for a battery while running a motor. Firstly, a model containing a PMSM motor, a battery and an inverter was constructed based on datasheet and experimental values. In the case of the battery, these parameters were estimated based on EIS data of a single cell. However, the parameters obtained left room for improvement, although not consequential for the results of the project as the battery model only served to prove the feasibility of the PRBS method. Secondly, a control structure was developed and tuned, containing both an inner current loop and an outer speed loop. It was shown that applying the PRBS in the d-current reference has minimal effect on the PMSM performance, since torque is primarily determined by the q-current. Consequently, it was paramount that the d-current controller must be fast since it needed to follow the PRBS signal.

It was then shown in simulation that applying PRBS only on a battery can be used to obtain the Nyquist plot in a given range. It was chosen for this project to implement a 4-bit and an 11-bit PRBS sequence using a sample time of 0.1 s and 0.001 s. These sequence combinations were chosen because they could produce maximum length sequence using the PRBS method. The 4-bit was used to prove the feasibility of the method in a simulation environment without large computational demands, while the 11-bit sequence served to obtain a higher resolution of impedances in the laboratory environment. Therefore, simulations using the inverter and motor were performed applying the 4-bit sequence under different scenarios. It was observed that the PRBS can be used to accurately estimate the Nyquist plot under stationary and operating conditions for a wide range of frequencies. However, when the i_q is present, distortions in I_{DC} appeared, making the PRBS less visible in it. To mitigate this, a gain of 2 was implemented on the PRBS signal, yielding a more visible PRBS behaviour.

In the laboratory, both the 4-bit and 11-bit sequences were implemented in both the stationary and operating conditions. It was found that the behaviour closely resembled simulation results although with a greater influence of noise in the system. It was also observed that when applying the PRBS, a ripple appeared on the speed, suggesting saliency in the motor. FFT analysis was performed on the DC current and voltage to obtain the Nyquist plots for the different scenarios. It was found that due to disturbances, both the 4-bit and 11-bit sequences yielded inaccurate results. However, due to the high resolution in the 11-bit sequence, it was possible to take the mean of every 30 points to obtain characteristic points of the Nyquist plot. Consequently, a curve was obtained for both the stationary and operating conditions, that closely matched the EIS data. However, due to the age of the cells under test, the points were shifted from the original data.

Therefore, it can be concluded that the online PRBS method can be used to obtain the Nyquist plot of a battery, although this method is sensitive to noise and limited by the dynamics of the system.

9. Future Work

In this chapter, other topics that could be investigated, or things that could be improved on in this project will be presented briefly.

9.1 Modelling of Battery

Choices were made during the modelling of the battery, which may influence the quality of the simulation results. This section will describe the possible impact of these choices.

9.1.1 Number of RC Branches

In this project, two RC branches were used in the battery model. More RC branches could be added in future to more accurately represent the battery.

9.1.2 Determination of Internal Battery Impedances

In this project, the internal battery impedance parameters are calculated as described in Chapter 4.1.1. There may be other methods which could represent the real battery model with more accuracy. As was seen in that chapter, the estimated parameters for the battery gave a Nyquist plot that described the high frequency behaviour well, while the low frequency behaviour differed a lot. A better fit for the battery curve would inevitably give a more realistic simulation, however this should not influence whether the PRBS method is valid.

9.2 Choices Regarding PRBS

This section describes the choices regarding the PRBS that should be investigated in the future.

9.2.1 Selection of the Type of PRBS

In this project, the specific PRBS structure is used is the MLBS, as described in Chapter 4.4.2. Other structures exist, that might give better results, but this was not investigated in this project. For industrial implementation, it would be necessary to investigate which PRBS type is the most suitable.

9.2.2 Single or Multiple PRBS Sequences

In this project, an eleven bits PRBS with sampling time 0.001 s is taken which is used for frequency spectrum between 0.5 Hz to 420 Hz. To observe the large frequency bandwidth, two PRBS structure can be taken since one with fewer numbers represent lower frequency spectrum and a larger number represents a higher frequency spectrum. By doing so, Nyquist plot can be obtained in a wider frequency band which allows to observe the battery behaviour in a wider range.

9.3 DC current controller

In this project, it was chosen to directly insert the PRBS signal on the d-current. However, perhaps a control structure could be developed to control the PRBS signal on the DC current to avoid the great amount of distortions, that occurred both in simulation and in the laboratory. This was not investigated in this project, but could be a topic for others to investigate in the future.

9.4 Applying PRBS While Charging

In this project, the idea has been to parametrise the battery while the motor is running. Something similar that might yield even better results could be to apply PRBS while the EV is charging. In this way, no disturbances from i_q would be present and it would be possible to apply PRBS on a wide range of SoC. Likewise, this scenario eliminate the need to mitigate speed disturbances, as the EV would be parked. To do this, it would be necessary to investigate what converters are present in-between the charging port of the EV and the battery to figure out whether this would be possible.

Bibliography

[1] European Commission. The eu transport sector and its contribution to reaching climate neutrality. https://climate.ec.europa.eu/eu-action/transport-decarbonisation/overview_en.

[2] Jussi Sihvo, Daniel-Ioan Stroe, Tuomas Messo, and Tomi Roinila. Fast approach for battery impedance identification using pseudo-random sequence signals. *IEEE Transactions on Power Electronics*, 35(3):2548–2557, 2020.

[3] Erik Schaltz. Aau micro course; lithium-ion battery modelling. https://www.moodle.aau.dk/course/view.php?id=50206. Visited: 10/09/2025.

[4] David A. Howey, Paul D. Mitcheson, Vladimir Yufit, Gregory J. Offer, and Nigel P. Brandon. Online measurement of battery impedance using motor controller excitation. *IEEE Transactions on Vehicular Technology*, 63(6):2557–2566, 2014.

[5] Nicola Campagna, Vincenzo Castiglia, Rosario Miceli, Rosa Anna Mastromauro, Ciro Spataro, Marco Trapanese, and Fabio Viola. Battery models for battery powered applications: A comparative study. *Energies*, 13(16), 2020.

[6] Gaizka Saldaña, José Ignacio San Martín, Inmaculada Zamora, Francisco Javier Asensio, and Oier Oñederra. Analysis of the current electric battery models for electric vehicle simulation. *Energies*, 12(14), 2019.

[7] Ana-Irina Stroe, Daniel-Ioan Stroe, Maciej Swierczynski, Remus Teodorescu, and Søren Knudsen Kær. Lithium-ion battery dynamic model for wide range of operating conditions. In *2017 International Conference on Optimization of Electrical and Electronic Equipment (OPTIM) & 2017 Intl Aegean Conference on Electrical Machines and Power Electronics (ACEMP)*, pages 660–666, 2017.

[8] Yuchao Wu and Balakumar Balasingam. A comparison of battery equivalent circuit model parameter extraction approaches based on electrochemical impedance spectroscopy. *Preprints*, September 2024.

[9] Jussi Sihvo, Tuomas Messo, Tomi Roinila, and Roni Luhtala. Online internal impedance measurements of li-ion battery using prbs broadband excitation and fourier techniques: Methods and injection design. In *2018 International Power Electronics Conference (IPEC-Niigata 2018 -ECCE Asia)*, pages 2470–2475, 2018.

[10] Tomi Roinila, Hessamaldin Abdollahi, and Enrico Santi. Frequency-domain identification based on pseudorandom sequences in analysis and control of dc power distribution systems: A review. *IEEE Transactions on Power Electronics*, 36(4):3744–3756, 2021.

[11] Minh Tran, Leevi Lignell, Jussi Sihvo, and Tomi Roinila. Implementation techniques for online impedance measurement of li-ion batteries. In *2023 IEEE Energy Conversion Congress and Exposition (ECCE)*, pages 168–173, 2023.

[12] Nadia O Laschuk, E Bradley Easton, and Olena V Zenkina. Reducing the resistance for the use of electrochemical impedance spectroscopy analysis in materials chemistry. *RSC advances*, 11(45):27925–27936, 2021.

[13] Abhijit Kulkarni, Hoda Sorouri, Yusheng Zheng, Xin Sui, Arman Oshnoei, Nicolai André Weinreich, and Remus Teodorescu. Li-ion battery digital twin based on online impedance estimation. In *2023 IEEE 17th International Conference on Compatibility, Power Electronics and Power Engineering (CPE-POWERENG)*, pages 1–6. IEEE, 2023.

[14] Measurement data for EIS test of AS1868117(LFP)(10Ah) Cell 1 at 5 degrees, provided by AAU Energy.

[15] AJ Fairweather, MP Foster, and DA Stone. Battery parameter identification with pseudo random binary sequence excitation (prbs). *Journal of Power Sources*, 196(22):9398–9406, 2011.

[16] Kaiyuan Lu. Dynamic modelling of electrical machines and control systems. https://www.moodle.aau.dk/course/view.php?id=51953. Visited: 11/09/2025.

[17] Art Pini. Use readily available components to generate pseudo-random binary sequences and white noise. https://www.digikey.dk/da/articles/use-readily-available-components-generate-binary-sequences-white-noise?srsltid=AfmBOopGVhk7BtgebGp4Q6CbrDwr-IA0rzIYRc-PcdVmEIXrIJKXQCKT. Visited: 29/09/2025.

[18] Ltd. A&S Power Technology Co. Specification provided by A&S Power Technology Co., Ltd. Lithium Iron Phosphate Battery for AS1868117(LFP)(10Ah) Cell.

[19] Texas Instruments, Incorporated. *InstaSPIN-FOC and InstaSPIN-MOTION User's Guide (Rev. I)*, 2022.

A. Parametrisation of PMSM

During this project, it was determined that the data sheet parameter values of the PMSM parameters could not be trusted, which meant that they had to be determined experimentally. This chapter will explain how the different parameters were determined.

I Determining Permanent Magnet Flux Linkage

In order to properly model the motor, it is necessary to know the permanent magnet flux linkage, λ_{mpm}, because is determines the relationship between torque and current and between voltage and speed. These relationships can be seen in Equations (4.19) and (A.1).

$$v_q = R_m i_q + \frac{d\lambda_q}{dt} - \omega(L_d i_d + \lambda_{mpm}) \tag{A.1}$$

The relationship shown in Equation (A.1) is going to be utilised when determining λ_{mpm} because all terms become zero except for v_q and $\omega\lambda_{mpm}$ when the motor is spinning and the terminals are open circuited. The procedure of determining the permanent magnet flux linkage is that the PMSM is connected to a DC motor on the rotors and voltage is applied to the DC motor. The speed of the motors and line-to-line voltage generated by the PMSM is then measured. The measurement is repeated 5 times, yielding the results shown in Table A.1.

Speed $[\frac{rad}{s}]$	RMS Voltage line-to-line [V]	RMS Phase Voltage [V]
73	4.94	2.58
84	5.72	3.30
96	6.4	3.69
105	7.18	4.15
116	8	4.61
126	8.54	4.93

Table A.1: Voltage and speed measurements from open circuit test

From these measurements, linear regression is performed between the speed and the phase voltage, with an intercept at the origin, to obtain the value for λ_{mpm}. This can be seen in Figure A.1.

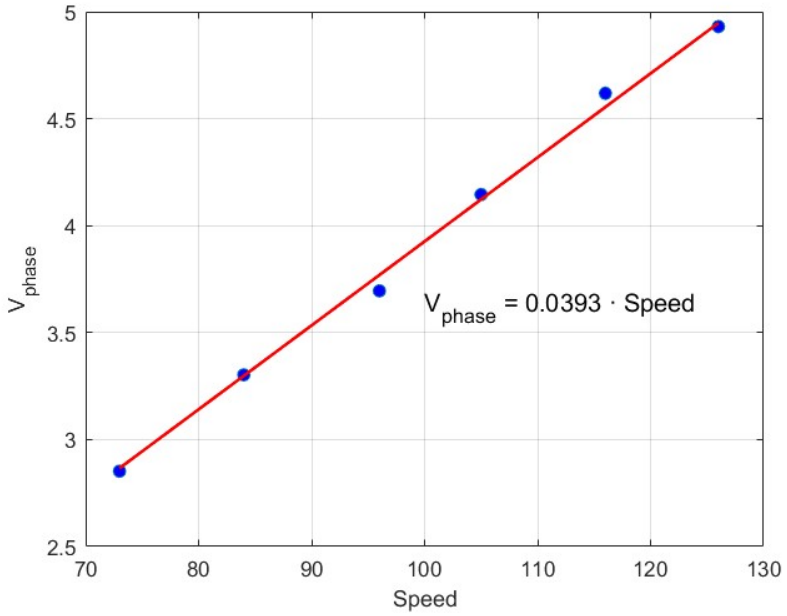

Figure A.1: Linear regression of voltage and speed measurements

Thus, from the equation displayed in Figure A.1, it can be seen that $\lambda_{mpm} = 0.0393$ Wb.

II Determining d- and q-axis Inductances

For both simulation and operation of the motor, it is necessary to have a good estimate of the d- and q- axis inductances, L_d & L_q, as they have a large influence on the currents. Therefore, a test was performed to determine these. To do the test, the motor was first aligned with phase a by shorting phases b and c and then applying a current through phase a. The motor was then blocked at this angle, such that it could not spin. Then a voltage step was applied and the current response was observed on the oscilloscope. Using this response, Equation A.2 could be solved for the inductance.

$$\tau = \frac{L}{R} \tag{A.2}$$

Here, τ is the time constant, L is the inductance and R is the resistance. The time constant measured was 2.88 milliseconds, and the resistance was found to be 0.357, yielding an inductance of 1.065 mH. As mentioned several times throughout the project, the motor is assumed to be non-salient, so this value is both the d- and q-axis inductance. If the motor was not assumed non-salient, the same test would have to be repeated with the angle shifted $\frac{\pi}{2}$ electrical radians.